oMEGACat. I. MUSE Spectroscopy of 300,000 Stars within the Half-light Radius of ω Centauri

M. S. Nitschai, N. Neumayer, C. Clontz, M. Häberle, A. C. Seth, T. -O. Husser, S. Kamann, M. Alfaro-Cuello, N. Kacharov, A. Bellini, et al.

The Astrophysical Journal, 958:8 (20pp), 2023 November 20 https://doi.org/10.3847/1538-4357/acf5db

oMEGACat. I. MUSE Spectroscopy of 300,000 Stars within the Half-light Radius of ω Centauri

M. S. Nitschai[1], N. Neumayer[1], C. Clontz[1,2], M. Häberle[1], A. C. Seth[2], T.-O. Husser[3], S. Kamann[4], M. Alfaro-Cuello[5,6], N. Kacharov[7], A. Bellini[6], A. Dotter[8], S. Dreizler[3], A. Feldmeier-Krause[1], M. Latour[3], M. Libralato[9], A. P. Milone[10], R. Pechetti[4], G. van de Ven[11], K. Voggel[12], and Daniel R. Weisz[13]
[1] Max Planck Institute for Astronomy, Königstuhl 17, D-69117 Heidelberg, Germany; nitschai@mpia.de
[2] Department of Physics and Astronomy, University of Utah, Salt Lake City, UT 84112, USA
[3] Institut für Astrophysik und Geophysik, Georg-August-Universität Göttingen, Friedrich-Hund-Platz 1, D-37077 Göttingen, Germany
[4] Astrophysics Research Institute, Liverpool John Moores University, 146 Brownlow Hill, Liverpool L3 5RF, UK
[5] Facultad de Ingeniería y Arquitectura, Universidad Central de Chile, Avenida Francisco de Aguirre 0405, La Serena, Coquimbo, Chile
[6] Space Telescope Science Institute, 3700 San Martin Drive, Baltimore, MD 21218, USA
[7] Leibniz Institute for Astrophysics, An der Sternwarte 16, D-14482 Potsdam, Germany
[8] Department of Physics and Astronomy, Dartmouth College, Hanover, NH 03755, US
[9] AURA for the European Space Agency (ESA), Space Telescope Science Institute, 3700 San Martin Drive, Baltimore, MD 21218, USA
[10] Dipartimento di Fisica e Astronomia "Galileo Galilei," Università di Padova, Vicolo dell'Osservatorio 3, Padova I-35122, Italy
[11] Department of Astrophysics, University of Vienna, Türkenschanzstrasse 17, A-1180 Wien, Austria
[12] Université de Strasbourg, CNRS, Observatoire astronomique de Strasbourg, UMR 7550, F-67000 Strasbourg, France
[13] Department of Astronomy, University of California, Berkeley, CA, 94720, USA
Received 2023 May 16; revised 2023 August 11; accepted 2023 August 28; published 2023 November 7

Abstract

Omega Centauri (ω Cen) is the most massive globular cluster of the Milky Way and has been the focus of many studies that reveal the complexity of its stellar populations and kinematics. However, most previous studies have used photometric and spectroscopic data sets with limited spatial or magnitude coverage, while we aim to investigate it having full spatial coverage out to its half-light radius and stars ranging from the main sequence to the tip of the red giant branch. This is the first paper in a new survey of ω Cen that combines uniform imaging and spectroscopic data out to its half-light radius to study its stellar populations, kinematics, and formation history. In this paper, we present an unprecedented MUSE spectroscopic data set combining 87 new MUSE pointings with previous observations collected from guaranteed time observations. We extract spectra of more than 300,000 stars reaching more than 2 magnitudes below the main-sequence turnoff. We use these spectra to derive metallicity and line-of-sight velocity measurements and determine robust uncertainties on these quantities using repeat measurements. Applying quality cuts we achieve signal-to-noise ratios (S/Ns) of 16.47/73.51 and mean metallicity errors of 0.174/0.031 dex for the main-sequence stars (18 mag $<\mathrm{mag}_{F625W}<$ 22 mag) and red giant branch stars (16 mag $<\mathrm{mag}_{F625W}<$ 10 mag), respectively. We correct the metallicities for atomic diffusion and identify foreground stars. This massive spectroscopic data set will enable future studies that will transform our understanding of ω Cen, allowing us to investigate the stellar populations, ages, and kinematics in great detail.

Unified Astronomy Thesaurus concepts: Galaxy nuclei (609); Globular star clusters (656); Star clusters (1567)

Supporting material: machine-readable table

1. Introduction

In recent years, we have been able to start decoding the formation history of our Galaxy, thanks to large spectroscopic surveys like the Gaia mission (Gaia Collaboration et al. 2016), APOGEE (Allende Prieto et al. 2008; Majewski et al. 2017), LAMOST/LEGUE (Deng et al. 2012) and GALAH (De Silva et al. 2015; Buder et al. 2021). These surveys, combined with the framework established through cosmological hydrodynamic simulations, have revealed the role that mergers have played in the Milky Way's formation history.

When less massive satellite galaxies merge with a larger host galaxy, several things happen: The tidal effects of the host galaxy will cause the smaller galaxy to disrupt and form stellar streams (Helmi & White 2001; Mayer et al. 2002). In addition, dynamical friction can cause the denser central regions of the smaller galaxy to sink toward the center of the host galaxy before being fully disrupted.

The Milky Way has had a quiet merger history, experiencing no recent major mergers (Stewart et al. 2008). The last significant merger happened around 10 Gyr ago with the Gaia-Enceladus satellite (e.g., Haywood et al. 2018; Helmi et al. 2018).

Most galaxies, including the Milky Way, contain a dense nuclear star cluster (NSC) at their center (Neumayer et al. 2020), the densest stellar systems known in the Universe. During a merger event, the NSC of the satellite galaxy will survive without being disrupted and live on in the halo of the host galaxy (e.g., Pfeffer & Baumgardt 2013).

NSCs in low-mass galaxies have very similar properties to massive globular clusters (Georgiev & Böker 2014; Neumayer et al. 2020), with half-light radii of 1–10 pc and masses of 10^6 to 10^8 $M_\odot$. Without their surrounding host galaxy, these stripped NSCs will look like massive globular clusters. Hence, they will be able to hide among the $\gtrsim$ 100 globular clusters in the galaxy. Recent semianalytic models predict 2–6 stripped

nuclei in the halo of the Milky Way (Pfeffer et al. 2014; Kruijssen et al. 2019). Because masses and star formation histories of NSCs track the galaxies they live in (e.g., Kacharov et al. 2018; Sánchez-Janssen et al. 2019; Fahrion et al. 2021), stripped nuclei can tell us about the masses of their original hosts and the times of merging if we can identify them.

An ongoing example of the galaxy merging process is the Sagittarius dwarf spheroidal galaxy, whose stars are wrapped in a stream around the Milky Way, created due to tidal stripping over the last several Gyr (Ibata et al. 1997; Laporte et al. 2018). The nucleus of this galaxy was discovered to be the globular cluster M54 long before the remainder of the galaxy was found. Detailed studies of M54 have revealed that, unlike a typical globular cluster (but typical of NSCs), it has stellar populations with a wide range of metallicities and ages (e.g., Siegel et al. 2007; Alfaro-Cuello et al. 2019).

Omega Centauri (ω Cen, NGC 5139) is the brightest, most massive globular cluster of the Milky Way ($\sim 3.55 \times 10^6\ M_\odot$, Baumgardt & Hilker 2018), sitting at a distance of only 5.43 kpc (Baumgardt & Vasiliev 2021). Due to the complexity of its stellar populations, it has long been suspected to be the stripped former nucleus of a galaxy that merged with the Milky Way a long time ago (e.g., Bekki & Freeman 2003). Evidence for the multiple populations of stars in the cluster comes from the multiple sequences in its color–magnitude diagram (CMD, e.g., Anderson 1997; Bedin et al. 2004; Bellini et al. 2010; Milone et al. 2017), a large spread in metallicity (e.g., Freeman & Rodgers 1975; Johnson & Pilachowski 2010), and possibly also in age (Hilker et al. 2004; Villanova et al. 2014). How prolonged the star formation in ω Cen was is still controversial, i.e., 4–5 Gyr Villanova et al. (2007) versus 1–2 Gyr Joo & Lee (2013). Additional evidence for the stripping scenario comes from kinematic information that finds the presence of a central stellar disk and a bias toward tangential orbits in the outer parts (van de Ven et al. 2006). ω Cen's status as a stripped nucleus has been further strengthened over the last decade through its association with stellar streams and the Gaia-Enceladus merger (e.g., Majewski et al. 2012; Ibata et al. 2019; Limberg et al. 2022). ω Cen is, therefore, our closest NSC, closer than our own Galactic center, and has much less extinction due to gas and dust. Due to its proximity, it has a large angular size, making it easily observable. For these reasons, ω Cen is the perfect laboratory for studying NSCs, stripped nuclei, and multiple populations. It can also inform us about the merger history of our galaxy since it is likely that its progenitor was part of one of the most massive early mergers of the Milky Way.

In order to study the cluster in detail and specifically the multiple populations, spectroscopic data are important for metallicity and abundance measurements. Due to the high crowding in the cluster, many spectroscopic surveys, like Gaia and APOGEE (Mészáros et al. 2021), are limited to a few bright stars, often only at the outskirts of dense clusters like ω Cen. Other studies like Johnson & Pilachowski (2010) and Johnson et al. (2020) have spectroscopic data covering the central region but only for the brightest stars. The largest spectroscopic survey for multiple Galactic globular clusters, including ω Cen, has been presented in Kamann et al. (2018). This survey covers the very center of the cluster, having thousands of spectra from the main sequence (MS) up to the red giant branch (RGB). We aim to further extend that sample out to the half-light radius.

The Multi-Unit Spectroscopic Explorer (MUSE) is the perfect instrument to investigate individual stars in clusters, as has been shown in other studies, e.g., Husser et al. (2016), Kamann et al. (2018), Alfaro-Cuello et al. (2019), Alfaro-Cuello et al. (2020), Kacharov et al. (2022). In this work, we present a large MUSE data set, covering ω Cen out to its half-light radius, and the spectroscopic analysis of hundreds of thousands of individual stars, by far the largest spectroscopic data set ever assembled for ω Cen, or in any cluster. The paper is divided into the following sections: In Section 2 we present the observations, and in Section 3 we describe the methods used to get the physical parameters for our catalog. In addition, in Section 4 we explain the analysis performed on that catalog to clean and test it. Further tests are also shown in the Appendix. Finally, in Section 5 we summarize and give an outlook on further works in progress using this catalog.

2. Data

2.1. Observations and Data Sets

The data presented in this paper were acquired with MUSE (Bacon et al. 2010, 2014), a second-generation Very Large Telescope (VLT) instrument located at the UT4 at the Paranal Observatory in Chile. Two sets of data are combined in this paper; the first are existing data, part of the MUSE guaranteed time observations (hereafter "GTO data"), with program IDs: 094.D-0142, 095.D-0629, 096.D-0175, 097.D-0295, 098.D-0148, 099.D-0019, 0100.D-0161, 0101.D-0268, 0102.D-0270, 0103.D-0204, 0104.D-0257, 105.20CR, and 109.23DV. These GTO data consist of 10 pointings with multiepoch data that have been analyzed already in several papers (Kamann et al. 2018; Husser et al. 2020; Latour et al. 2021) as well as six central pointings using the MUSE narrow field adaptive optics mode (NFM), presented in Pechetti et al. (2023). The second data set is from General Observer (GO) program 105.20CG.001 (PI: N. Neumayer); this includes 87 new MUSE pointings taken between 2021 February and 2022 September. We refer to this data set as the "GO data" and describe this data set in more detail below.

MUSE is an integral-field spectrograph based on image slicing with 24 identical integral-field units (IFUs). The field of view in the wide field mode (WFM), which was used for the GO data, is $59\farcs9 \times 60\farcs0$ for each pointing with a spatial pixel scale of $0\farcs2$ pix^{-1}. The instrument observes in the optical domain (480–930 nm) with a resolving power increasing with wavelength from 1770 to 3590 and a spectral sampling of 0.125 nm pix^{-1}. For the GTO NFM data, the field of view of each pointing is $7\farcs5 \times 7\farcs5$, they have a sampling of $0\farcs025$ pix^{-1} and the resolving power is increasing with a wavelength from 1740 to 3450. In both the GO and GTO data, some central pointings are also taken using the VLT Adaptive Optics Facility (AOF; Arsenault et al. 2010; Ströbele et al. 2012). In adaptive optics (AO) mode, the NaD lines are blocked using a filter, causing a gap in the spectra between 580 and 597 nm (Weilbacher et al. 2016).

In the GO data, each field has three exposures with a rotation of 90° between them (no dithering), and the exposure time was 200 s. The observations were requested in service mode at an airmass less than 1.4 and a seeing better than $0\farcs8$. These conditions were almost always fulfilled; see Table 2 in the Appendix for more details on the observing conditions. We note that one observing block (OB 1.3) was initially observed

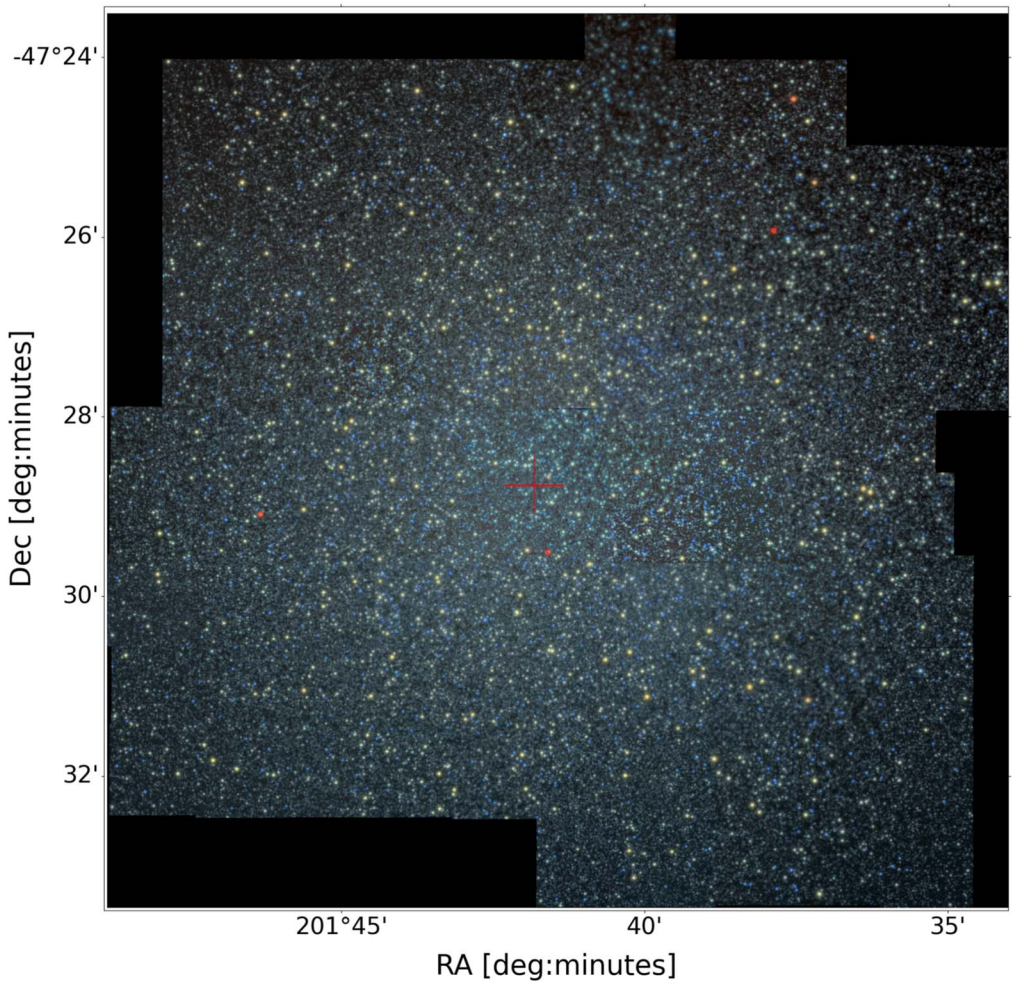

Figure 1. Image of ω Cen. A three-color RGB image of ω Cen created from MUSE WFM data using synthetic SDSS i, r, and g filters. The image displays the coverage of all WFM data (both GTO and GO). The red cross indicates the center of the cluster.

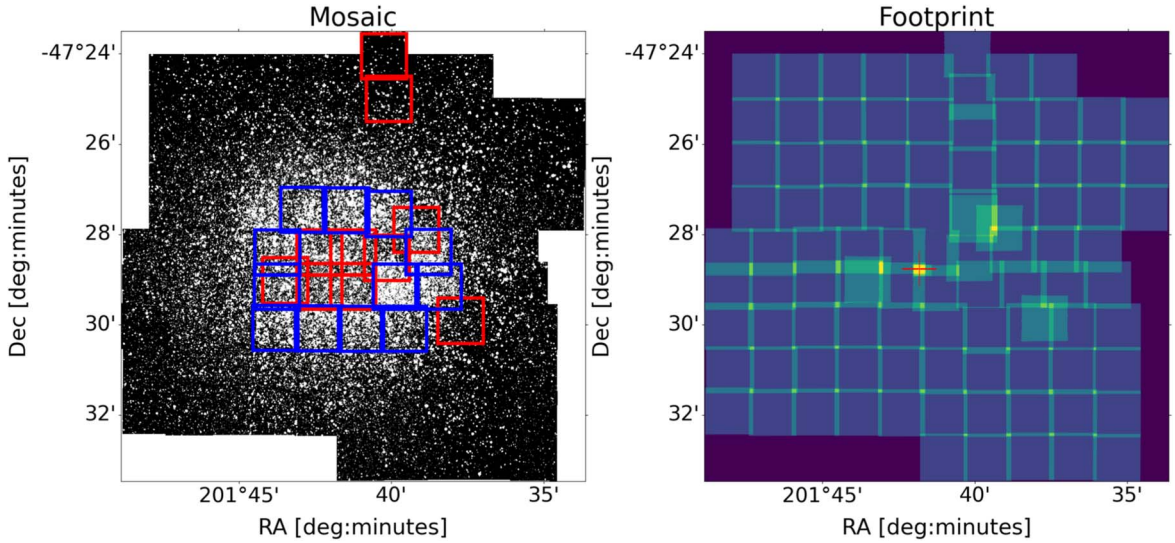

Figure 2. Image of ω Cen and footprint of the MUSE pointings. On the left is a gray-scale image created from the combined GO and GTO MUSE WFM data. Overlaid blue colored squares indicate the GO AO pointings, red squares the WFM GTO data, while the region without squares is where the non-AO GO WFM pointings lie. On the right is the footprint of the individual pointings showing the overlap of the data. At the center of the right-hand figure, the NFM data are within the yellow region at the center of the image, indicated with a red cross.

using AO with the wrong offset, causing a small gap in our data set. Therefore, it was repeated without AO in 2022 September once more, to fill in the gap.

We show the spatial coverage of our combined data set in Figures 1 and 2. The combined data set includes a total of 97 WFM pointings as well as six central NFM pointings,

providing complete coverage out to the half-light radius of ω Cen (4.′65 or 7.04 pc, Baumgardt & Hilker 2018).

The reduction and analysis of the GTO data were already done; details on the GTO WFM data are presented in Kamann et al. (2018), while the NFM data are presented in Pechetti et al. (2023). For the GO data, we duplicated the GTO WFM reduction procedure as closely as possible.

For the rest of the paper, most of the data reduction and analysis steps refer to just the GO data, except where clearly specified to also include the GTO data.

2.2. Data Reduction

We use the MUSE pipeline, version 2.8.3 (Weilbacher et al. 2016, 2020), to reduce the GO data. This pipeline uses CPL (Streicher 2016) and the ESOREX (ESO CPL Development Team 2015) packages and contains all necessary procedures for the data reduction process, including bias subtraction, flat-fielding, illumination correction, and wavelength calibration. Further, the pipeline flux calibrates the exposures using a standard star, corrects for the barycentric motion of the Earth, and combines the three single exposures into one for each field. We use the default settings for most parts of the pipeline, except for sky subtraction, where we use a sky continuum file containing zeros as the model, so that only the emission lines are subtracted, but not the sky continuum. Removing the sky continuum would also remove starlight in a crowded region like ours since even the darkest spaxels still contain starlight. This will leave the sky continuum in our final data cubes, but since we do a point-spread function-based extraction (see Section 3.1), these emissions will not be in the spectra we extract but in the background components determined during the extraction.

In addition, we are not doing any Raman correction since the field of view is too crowded or the Telluric correction, since our spectral fitting routine can remove them better. Hence, the Telluric lines are included in our spectral fit and are removed from the spectra; see Section 3.3.

The total MUSE data coverage is shown in Figure 2, where the red squares indicate where the WFM GTO pointings lie and the blue squares where the 12 new WFM-AO pointings are, while all other pointings are WFM without AO, 75 in total. The GTO NFM data are within the yellow region at the center of the right panel of Figure 2 (the small yellow square where the red cross lies). The gaps in our GO pointings, visible in Figure 3, in the center and upper part of the image are filled in with the GTO pointings so that we have full coverage of the cluster without gaps when combining the two data sets.

3. Analysis Methods

After the reduction of the MUSE mosaic, the next step is to get spectroscopic information for individual stars. Therefore, we need to extract the spectra of individual stars and measure physical parameters from these spectra.

3.1. Spectral Extraction

To extract individual spectra for the stars in the MUSE fields we use PAMPELMUSE[14] (Kamann et al. 2013) and the Hubble Space Telescope (HST) catalog from Anderson & van der Marel (2010). PAMPELMUSE takes the photometry and position of the stars in the HST catalog as a reference for the stars in the field of view of the MUSE data. It fits the point-spread function (PSF) as a function of wavelength. Forced PSF photometry performed at each wavelength for all the stars in the catalog allows PAMPELMUSE to separate sources efficiently, even in crowded regions. The Anderson & van der Marel (2010) catalog includes F625W and F435W magnitudes for 1.2×10^6 stars and covers a field of $10' \times 10'$ with a pixel scale of 50 mas pix^{-1}. We use a Moffat profile (Moffat 1969) for the PSF as defined in Section 4.2 of Kamann et al. (2013) and allow it to vary its ellipticity, positional angle, β-parameter, and FWHM, while the initial value for the FWHM is set to be the mean value of the seeing at the time of the observation. The extracted spectra also get a quality flag assigned from PAMPELMUSE where 0 is the best flag a spectrum can get. While there are four other criteria for the flags, there can also be a combination of them: 1, more than one source contributing; 2, signal-to-noise ratio (S/N) < 10; 4, the flux is negative; and 8, the centroid of the source is outside the field of view of the data cube).

We have performed an additional analysis on some OBs using a different extraction setup and found that the final results for spectra with an S/N >10 do not change significantly; see Appendix B. In Section 3.2we show the completeness of this extraction for the GO data set.

In total we extract with PAMPELMUSE 355,682 stars from the GO MUSE data set, see Figure 3, where we show their positions.

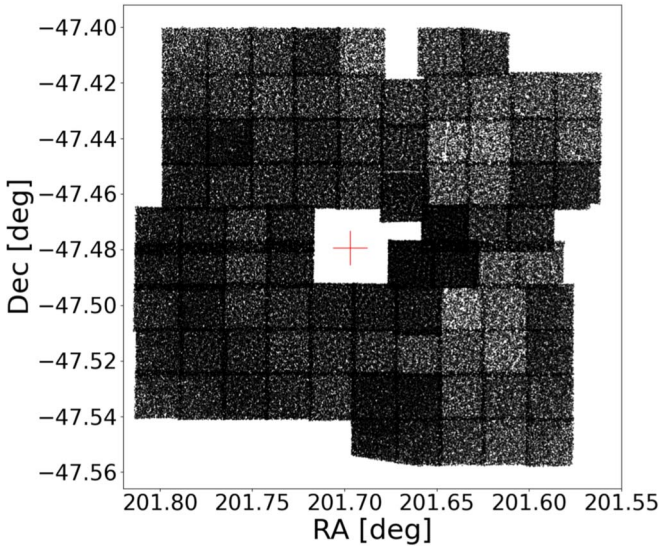

Figure 3. All extracted GO stars. The figure shows the positions of all extracted GO stars using the Anderson & van der Marel (2010) photometric catalog. The red cross indicates the center, while the holes at the top and at the center are later filled with the GTO stars. Some edges are cut off because the Hubble Space Telescope footprint does not perfectly cover the MUSE footprint. The overlap regions are denser, since more stars are observed due to the fact that there are two or more exposures. The variation in the number of stars seen in different fields is due to varying observing conditions that impact our completeness.

3.2. Completeness

We investigate how complete our GO data are after the spectral extraction compared to the HST catalog (Anderson & van der Marel 2010).

[14] https://PampelMuse.readthedocs.io/en/latest/about.html

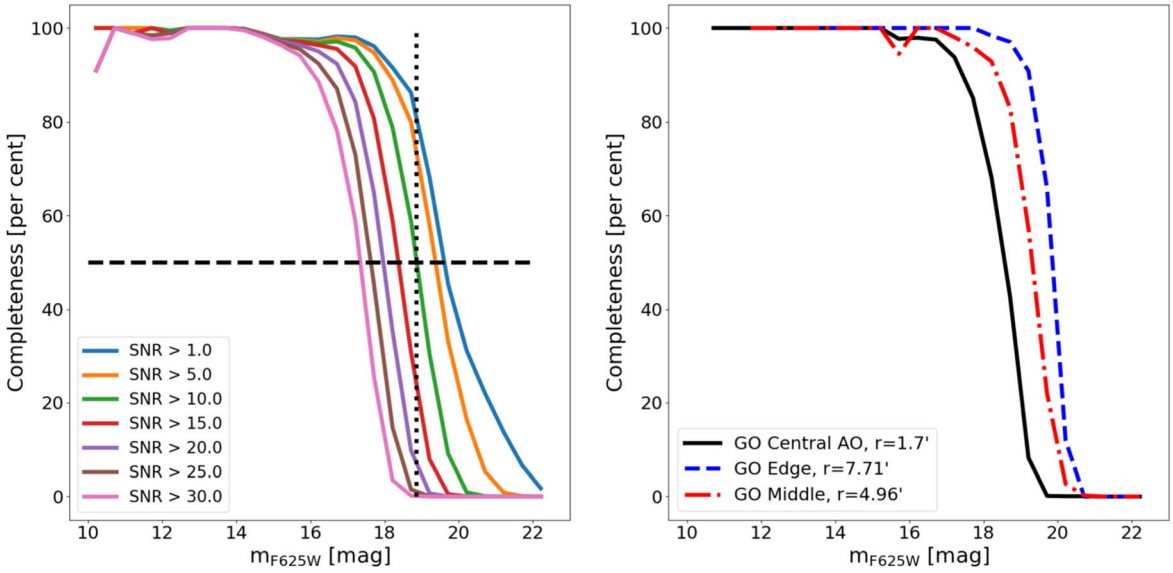

Figure 4. GO Completeness plots. On the left is the overall GO completeness (the combined completeness for all 87 GO pointings) for different S/N cuts, from left to right, the S/N is decreasing. The dashed line indicates 50% completeness, and the dotted line is 18.86 mag in F625W. The right plot shows for an S/N > 10 the individual completeness for three pointings at different radii from the center.

For each MUSE pointing we mask the edges of the pointings by 5″, in order to not get edge effects, and we divide our sample into 0.5 mag-wide bins and define the completeness in each bin as the ratio between the number of stars in the HST catalog and the number of stars for which we actually extract a spectrum from the MUSE data. We computed the completeness excluding spectra with an S/N lower than specific thresholds, i.e., 1, 5, 10, 15, 20, 25, and 30.

We show the overall completeness curves as a function of magnitude for different S/N cuts in the left panel of Figure 4. The completeness is almost 100% for the brightest stars and falls off toward fainter stars. The left panel shows that the overall completeness is above 50% for stars brighter than ∼18.86 mag (F625W Filter) for an S/N threshold of 10, while for higher S/N, this is shifted to lower magnitudes. The right panel shows that in the central regions, the completeness is lower for the fainter stars due to crowding.

3.3. Spectral Fitting

After extracting the spectra, we use SPEXXY[15] version 2.5 to measure the physical parameters of the stars. The observed spectra are compared to synthetic spectra from the Phoenix library (Husser et al. 2013) to derive each star's effective temperature $T_{\rm eff}$, and metallicity [M/H] using a χ^2 minimization. The range of the spectral parameters are: -4 dex $\leqslant$[M/H] $\leqslant 1$ dex, 2300 K $\leqslant T \leqslant$ 15,000 K and $0 \leqslant \log(g) \leqslant 6$. We also include a SPEXXY fit to the telluric absorption lines (which were not corrected previously; see Section 2.2) for H_2O and O_2. We use all spectra we could extract in this analysis part regardless of their quality at this point.

The initial values for log(g) and $T_{\rm eff}$ were determined as outlined in Husser et al. (2016); Kamann et al. (2018). In summary, the photometry from Anderson & van der Marel (2010) was fitted with an isochrone from the PARSEC database (Marigo et al. 2017), and each observed star was assigned the stellar parameter from the nearest isochrone point in the magnitude–color plane. For that, a 2D polynomial is fitted to the temperature and log(g) from the isochrone as a function of color and magnitude. This isochrone has an age of 13.7 Gyr, a metallicity of -0.94 dex, extinction ($A_{\rm v}$) of 0.23 mag, a distance of 5320 pc, and is shown as yellow dots in Figure 5. Since it is known that ωCen has multiple populations, one isochrone is not ideal to describe all populations, but here we only want to get initial values and a reliable log(g) for our spectral fit. A detailed population analysis will follow in upcoming work. The same is true for binary stars or multiple stellar systems, which are also offset in the color–magnitude diagram (CMD). However, the binary fraction of ωCen is small, less than 5% (Elson et al. 1995; Mayor et al. 1996) and in recent work even lower at $2.70\% \pm 0.08\%$ (Bellini et al. 2017b) and because of multiple populations, the binary sequence is also intertwined with the main-sequence track. Since log(g) does not strongly affect the [M/H] determination (see also Section C.1 Husser et al. 2016; Kamann et al. 2016) and we only require reliable log(g) parameters, one isochrone is sufficient even if the cluster is much more complex. We show the CMD in Figure 5. During the fit with SPEXXY, log(g) is fixed to the value provided by the isochrone ranging from 0 to 6, the α-enhancement is kept constant at $[\alpha/{\rm Fe}] = 0.3$ dex (similar to Latour et al. 2021), while $T_{\rm eff}$ and [M/H] are determined. SPEXXY also measures the line-of-sight (LOS) velocity, $v_{\rm los}$, for the observed spectra. For that, we need initial values, which we get from a first cross correlation with templates before starting the run with SPEXXY. If the result of the cross correlation is not good enough, and we obtain $r_{\rm cc} \leqslant 4$ from the r-statistics (Tonry & Davis 1979), we set the initial value to 234 km s^{-1}, which is the mean LOS velocity of the whole cluster (Baumgardt et al. 2019).

For the spectral fit, we use the whole wavelength range of the MUSE spectra, excluding only the NaD line or AO region (578–599 nm) and any other bad pixels identified. Four example spectra are shown in Figure 6 together with their best-fitting template spectrum in red. The light red shaded areas are the masked regions excluded from the fit. In addition, the S/N

[15] https://github.com/thusser/spexxy

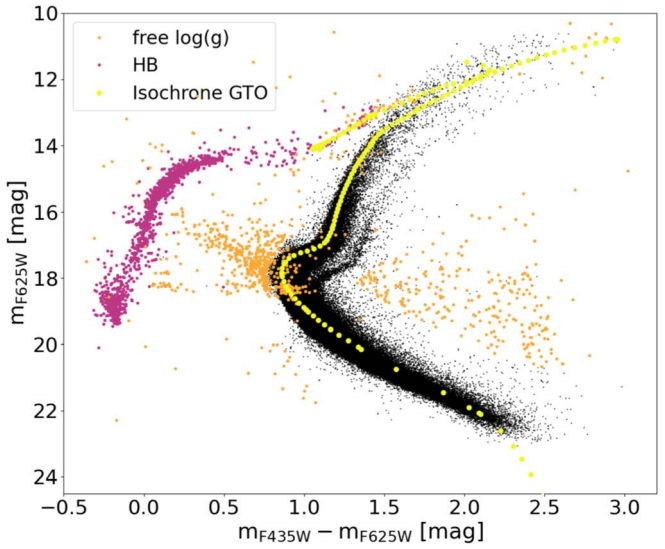

Figure 5. CMD of GO stars. CMD of the stars in the GO data set. The black dots show the stars with fixed log(g) in our SPEXXY fit while the orange points have free log(g), and the purple are the horizontal-branch stars, which are disregarded in the current analysis. The yellow points indicate the position of the isochrone used to infer the log(g).

is also determined by SPEXXY from the fit residuals providing a good indicator of the quality of the data.

In summary, with SPEXXY we derive values for [M/H], v_{los}, T_{eff}, S/N, telluric parameters, and their statistical errors. However, the results for stars lying further away from the isochrone (e.g., blue stragglers sequence (BSS) or asymptotic giant branch stars (AGB)) that is used to provide the log(g) values have to be considered biased. Hence, for stars not lying on the main isochrone, i.e., stars indicated with orange dots in Figure 5, we rerun SPEXXY allowing the log(g) parameter to vary freely during the fit. These stars are either not following the main CMD track (these might be nonmember stars or have unreliable photometry measurements from HST) or belong to the BSS or AGB. For stars that could be BSS/AGB or be part of the main CMD track, we keep both sets of values with free and fixed log(g). These are the orange dots that lie on top of the black dots in Figure 5. This increases the number to 356,065 measurements due to the duplicates added from the overlap regions.

For further analysis, we do not include the horizontal-branch (HB) stars, indicated as purple dots in Figure 5. Stars hotter than ∼11,000 K have chemically peculiar atmospheres due to diffusion and require dedicated model atmospheres for proper analysis (see Latour et al. 2023). The analysis of the HB stars included in our GO data will be presented elsewhere.

4. Analysis

In Section 3 we explained how we get a spectroscopic catalog from our MUSE data. This catalog needs to be further analyzed to remove contamination from foreground/background stars and to obtain robust measurements. Our overall goal is to keep as many stars as possible in the catalog and provide all parameters needed to perform the relevant quality cuts depending on the science case.

For our final catalog, we combine both the GO and GTO data sets. The GTO catalog contains 795,944 measurements belonging to 75,416 unique stars (see Section 4.3). As described in Section 3, the GO analysis followed that of the GTO data with three main differences: (1) the GTO data have multiple epochs of observations as opposed to a single epoch for the GO data, (2) the GTO uses two HST catalogs for source positions, the catalog created by Anderson et al. (2008) for the Advanced Camera for Surveys (ACS) survey of Galactic GCs (Sarajedini et al. 2007) and the Anderson & van der Marel (2010) catalog, and (3) during SPEXXY fits the log(g) for the BSS in the GTO data set was kept fixed to 4.2 dex, while we fit for log(g) for these stars.

4.1. Reliability Parameter

To have one overall parameter evaluating the quality of the derived LOS velocities, we calculate a reliability parameter R, as explained in Section 3.2 of Giesers et al. (2019):

$$R = (2R_{S/N} + 10R_{cc} + R_{\epsilon_{vcc}} + 3R_{v} + 2R_{\epsilon_{v}} + 5R_{v=vcc})/23. \quad (1)$$

The different components can be either false (0) or true (1), allowing the range of R to be from 0 to 1, with higher values being more reliable than lower ones. The first component, $R_{S/N}$, is an S/N cut, while the other parameters are different checks of the credibility of the LOS velocity calculations. In detail, they check the quality of the cross correlation (R_{cc}), if the cross correlation and the full-spectrum fit uncertainty are plausible ($R_{\epsilon_{vcc}}$ & $R_{\epsilon_{v}}$), if the full-spectrum fit velocity agrees with the expected cluster or foreground velocity and with the cross correlation (R_{v} & $R_{v=vcc}$).

First, we consider a minimum S/N of 5 to be reliable:

$$\boldsymbol{R}_{S/N} = S/N \geqslant 5. \quad (2)$$

That is, however, not our suggested S/N cut for the whole catalog, which should be higher (Section 4.7), but only for the velocity calculation, which does not need that high S/N. In addition, we use the FWHM result from our cross correlation and the r-statistics (Tonry & Davis 1979) to check the quality of the cross correlation which gave the initial LOS velocities for the fit with SPEXXY:

$$\boldsymbol{R}_{cc} = r_{cc} \geqslant 4 \;\&\; \mathrm{FWHM} > 10\ \text{Å}. \quad (3)$$

Further, a plausible velocity uncertainty of 0.1 km s^{-1} for the velocity from SPEXXY and from the cross correlation is required:

$$\boldsymbol{R}_{\epsilon_{v}} = \epsilon_{v} > 0.1\ \mathrm{km\ s^{-1}} \quad (4)$$

$$\boldsymbol{R}_{\epsilon_{vcc}} = \epsilon_{vcc} > 0.1\ \mathrm{km\ s^{-1}}. \quad (5)$$

Additionally, the velocity output from SPEXXY should be plausible. This means that it should match the velocity of either the cluster or the Galactic field stars. Hence, the values are checked to be within 3σ of the cluster velocity and the cluster dispersion, $v_{cl} = (232.7 \pm 0.2)$ km s^{-1} and $\sigma_{cl} = 17.6$ km s^{-1} (Baumgardt & Hilker 2018), or that they agree with the foreground stars. For the cluster membership, we calculate:

$$R_{v_1} = \frac{|v - v_{cl}|}{\sqrt{\epsilon_{v}^2 + (\sigma_{cl} + \epsilon_{v_{cl}})^2 + a^2}} \leqslant 3. \quad (6)$$

With a being 30 km s^{-1} which is added to the broadening in order to account for the orbital motions of binary stars, as their measured velocities would not necessarily be covered by the

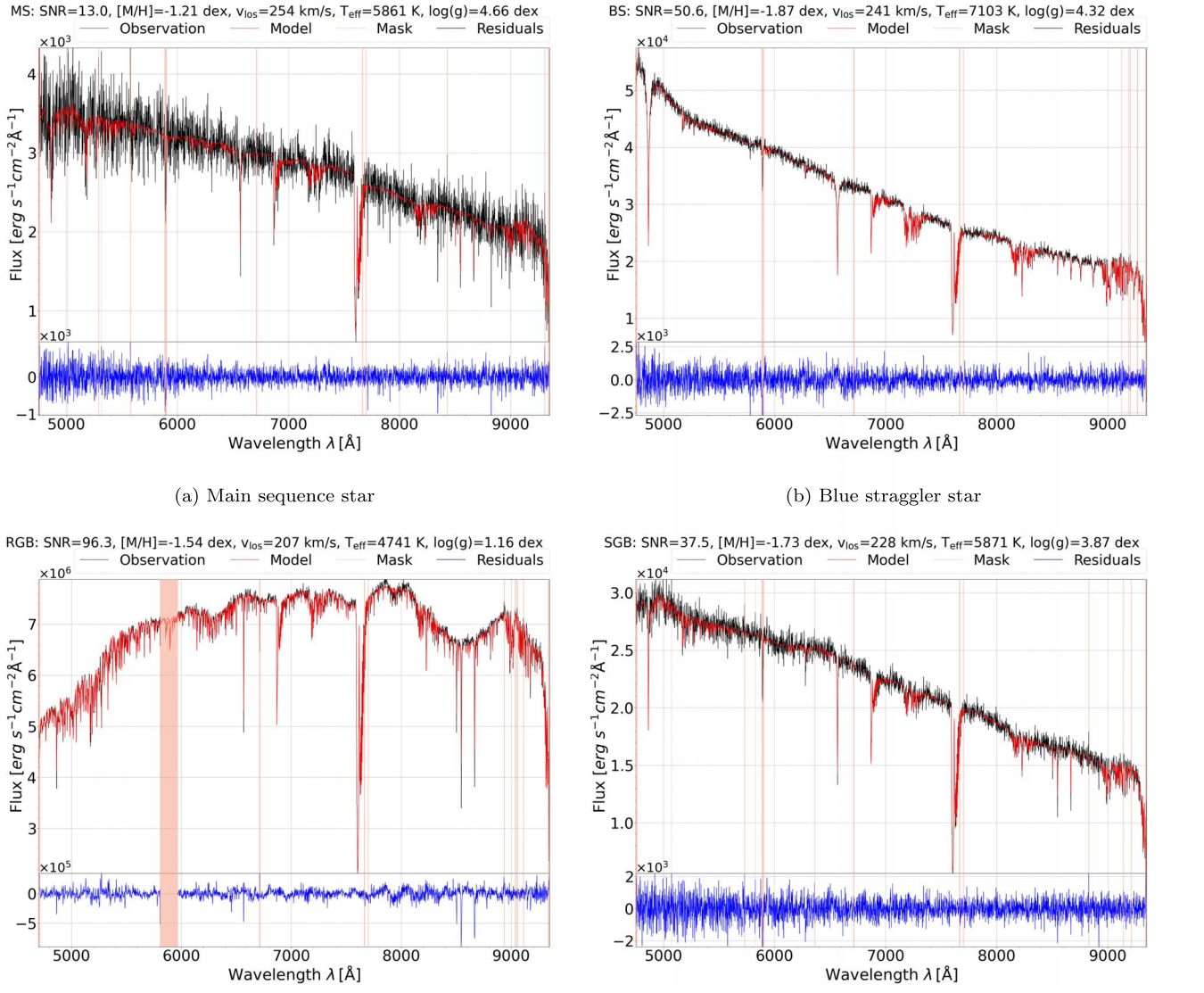

(a) Main sequence star

(b) Blue straggler star

(c) Red giant branch star

(d) Subgiant branch star

Figure 6. Example spectra. (a)–(d) Spectra of stars at different stages of evolution plotted in black, with best-fitting SPEXXY models in red. The light red shaded areas are the excluded/masked regions during the fit. Note that the RGB star (d) is observed with AO, and the NaD line is blocked. The bottom panels show the data model residuals in blue. We note that the deep broad absorption features at 6800 and 7600 Å are telluric features that are fit by SPEXXY along with the stellar properties. The best-fitting parameters for S/N, [M/H], v_{los}, T_{eff}, and the log(g) value are given on top of each spectrum.

cluster distribution. For the foreground stars:

$$R_{v_2} = \frac{|v - 0\ \mathrm{km\ s^{-1}}|}{\sqrt{\epsilon_v^2 + (50\ \mathrm{km\ s^{-1}})^2}} \leqslant 3, \tag{7}$$

with 50 km s^{-1} being the estimate for the foreground stars from the Besançon model (Robin et al. 2003) used in Section 4.4. The total R_v is true if at least one of the $R_{v_{1,2}}$ is true. Similarly, a maximum 3σ difference is allowed between the cross correlation results and the final SPEXXY results while allowing a maximal velocity error of 40 km s^{-1} for the cross correlation:

$$\boldsymbol{R}_{v=\mathrm{vcc}} = \frac{|v - v_{\mathrm{cc}}|}{\sqrt{\epsilon_v^2 + \epsilon_{\mathrm{cc}}^2}} \leqslant 3. \tag{8}$$

We include the total R parameter for all stars in the catalog.

4.2. Error Analysis

To get a better understanding and estimate of the errors on our fitted parameters, we use stars with multiple observations (see Section 4.3), allowing us to compare the different results we get for the same star, similar to Husser et al. (2016) and Kamann et al. (2018). From that, we can compare the statistical uncertainty we get from the spectral fitting routine with the scatter from the repeat measurements. This allows us to estimate how accurate the errors from the spectral fitting routine are, and any scaling factor needed to correct them. We do this analysis for our main results from SPEXXY: the metallicity, line-of-sight velocity, and effective temperature, using only the individual measurements used to compute the mean parameters, as described in Section 4.3 for the error analysis.

We calculate:

$$\Delta y = \frac{y_i - y_j}{\sqrt{\epsilon_i^2 + \epsilon_j^2}},\ i \neq j \tag{9}$$

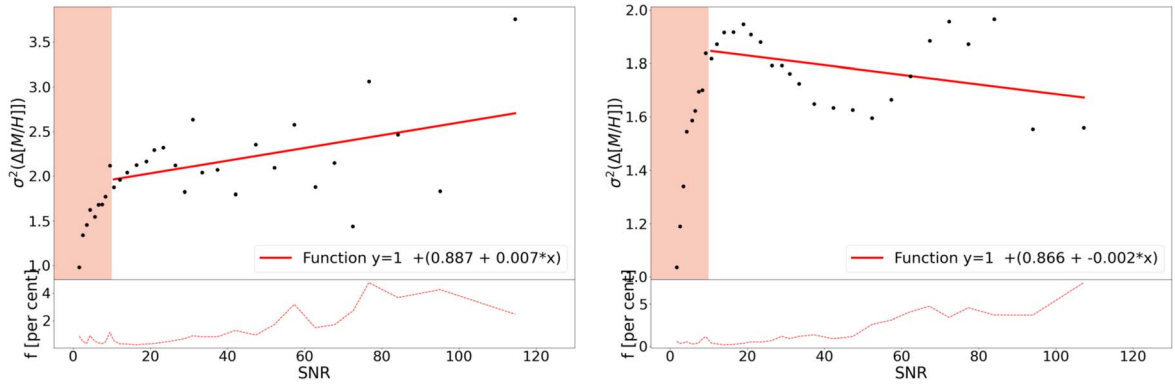

Figure 7. Error analysis correction. Top panels: the x-axis is the S/N, and the y-axis is the σ^2 of the Δ[M/H] for the GO data on the left and the GTO data on the right. The red line is the best-fitting first-order polynomial, the black dots are our data values, and the light red shaded area is the region below an S/N of 10, which we exclude from the analysis. Bottom panels: the x-axis is the S/N and the maximum percentage of counts one star has in each bin. The red dashed line shows the maximum number of measurements each star can have, which is clearly always below 10% of the total number of measurements in each bin, making sure the statistics in each bin are not the result of only one star.

where y_i, y_j are the different results we get from SPEXXY (where y = [M/H], v_{los} or T_{eff}) for the same star in two different observations, and ϵ_i, ϵ_j are their SPEXXY errors. Some stars are in more than two observations (maximum in four for the GO data, 66 for the GTO data), so we calculate Δy for each combination of different results, giving us 24,216 values for the GO data set and 2,016,633 for the GTO.

Afterward, we bin all Δy values in S/N bins depending on the mean S/N of the two measurements, SN_i and SN_j. We defined the S/N bins so that for the GO and GTO data, the statistics of no S/N bin can be dominated by just one star with multiple measurements if placed in the same bin. In the bottom panel of Figure 7 we show the maximum percentage of counts (f = max[counts one star]/total number counts, per bin) one star has in each bin, whereas for the GO data, it is always below 5% and for the GTO below 10 %. The distributions of Δy in each of the S/N bins, if the SPEXXY errors are accurately estimated, should be a Gaussian with $\sigma = 1$ and the mean at 0.

In Figure 8 we show an example of the cumulative distribution for the metallicity errors before any correction (black solid line) in comparison to a normal distribution (red line). We find that, as in this example for S/N $>$ 10, the SPEXXY errors typically are underestimated relative to the repeat measurements, which are a better estimate of the true errors. We, therefore, multiply the SPEXXY errors by a scaling factor, $\sqrt{1 + g(S/N)}$, to get more accurate errors for each star. After applying the scaling of the errors (see next paragraph), the cumulative distribution of the repeat measurement Δ[M/H] (black dashed line in Figure 8) follows the normal distribution."

If we plot the variance σ^2 (σ calculated as half of the difference between the 15.86 percentile and 84.14 percentile) of this distribution as a function of S/N, we can see that σ^2 is higher than 1 toward larger S/N, see Figure 7. We can describe this trend using a simple function, $y = 1 + g(x)$, with g(x) being a linear function, in order to get an estimate of the error correction needed as a function of S/N. We exclude the S/N bins below 10 for the fitting of the line. In Table 1 we list the best-fitting parameters for the scaling relation and the values for the maximum and minimum scaling for S/N $>$ 10. To quantify how accurately the linear function captures the repeat measurement data, we also include the maximum/minimum

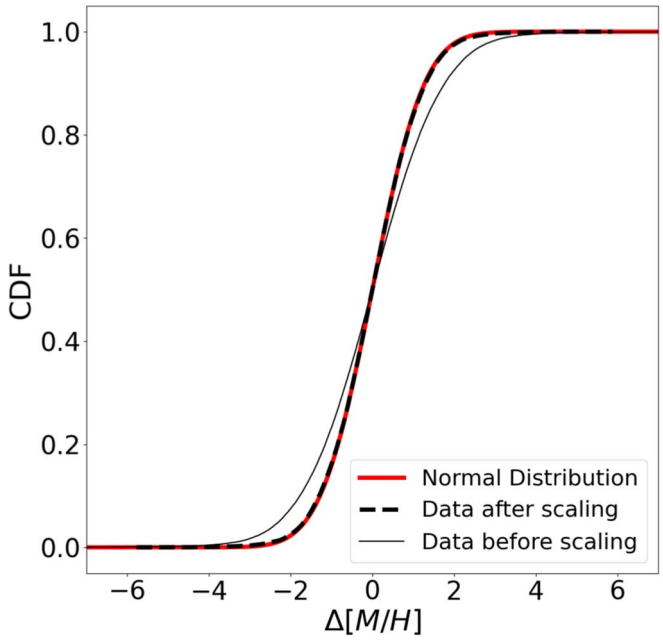

Figure 8. Error analysis CDF. The cumulative distribution of the Δ[M/H] in black for S/N $>$10 for the GO data and in red the distribution if it was a normal distribution. The dashed black line is the distribution after the error correction.

fractional residual to this fit (i.e., the fractional error on the point that lies farthest from the line in Figure 7).

The derived scaling functions are then applied to all data according to their S/N. The mean scaled errors for 40 $<$ S/N $<$60 are $\epsilon_{v_{los}} = 3.11$ km s^{-1}, $\epsilon_{T_{eff}} = 36$ K and $\epsilon_{M/H} = 0.057$ dex. These new, scaled errors are more accurate estimates of the true errors, and hence we will always use them in the following analysis.

4.3. Combining Multiple Measurements

The next step is to combine measurements for each observed star. Due to the multiple epochs of observations in the GTO data, each star has been observed multiple times, and the spectra were analyzed independently, such that the 795,944 measurements belong to 75,416 unique stars. For the GO data, only stars in the overlap regions of the different pointings (green and yellow regions in Figure 2) have been observed more than once, with 303,822 unique stars out of the 356,065

Table 1
Error Analysis

Data Set Parameter	a	b	Maximum Scaling Model/Data	Minimum Scaling Model/Data	Maximum Fractional Residual	Minimal Fractional Residual
GO [M/H]	0.887	0.007	1.644/1.938	1.401/1.200	0.179	0.226
GO v_{los}	−0.143	0.062	2.819/2.943	1.229/1.351	0.243	0.186
GO T_{eff}	1.791	−0.003	1.639/1.701	1.292/1.213	0.279	0.169
GTO [M/H]	0.866	−0.002	1.359/1.402	1.293/1.246	0.071	0.051
GTO v_{los}	−0.137	0.009	1.354/1.346	0.979/0.982	0.022	0.021
GTO T_{eff}	1.463	−0.014	1.521/1.596	0.976/1.137	0.209	0.125

Notes. Column 1 is the data set and parameter used for the error analysis. Columns 2 and 3 are the best-fitting parameters for the first-order polynomial, $g(x) = a + b \cdot x$, where x is the S/N and y is the $\sigma^2(\Delta y)$. Columns 4 and 5 are the maximum/minimum scaling we get from our best fit and what the actual data have. Columns 6 and 7 are the maximum and minimum fractional residuals, which are always under 30%.

measurements. In addition, there are also overlapping regions in the GTO and GO data where stars are in both data sets.

To combine multiple measurements of stars, we do a mean calculation for both data sets together after scaling the errors. First, we require the measurements to have a successful SPEXXY fit, meaning a fit to the templates could be performed without problems, and the final parameters are not close to their limits set for the fit. These cuts leave us with 744,344 GTO measurements and 335,834 GO measurements.

For stars with multiple measurements, we then calculate the mean values using a subset of measurements selected in a procedure based on their reliability value (Section 4.1), magnitude accuracy from the spectral extraction, the distance to the edge of the detector, and an S/N cut. We use a threshold reliability value of 0.5, and magnitude accuracy (the relative accuracy of the magnitude from the extracted spectrum versus the HST catalog) <0.6. We continue with measurements that meet these thresholds, or if there are none for a single star, we keep all measurements for the next steps in the combination.

Next, to use comparable measurements in the mean calculation, we first find the highest S/N spectrum and check if it is at least 5 pixels (1″) away from the edge of the pointing. If it is, we consider it the best measurement for the given star. If it is not, we check the second-highest S/N spectrum and set that as the best measurement or, if it is also too close to the edge, we return to the highest S/N spectrum as the best measurement. Having found the best measurement, we require all remaining measurements to have at least half the S/N of the best measurement or, in general higher than 20, at least as good of an extraction quality flag as the best, and if the best measurement was more than 5 pixels away from the edge, the other measurements have to be, too. The measurements that pass these tests are in general comparable to the best measurement and are used to calculate the mean measurements for a given star. If there is only one measurement, then that is used as a single entry for that star.

For the mean calculation of [M/H], v_{los} and T_{eff} we calculate the inverse-variance weighted mean, using the scaled errors (see Section 4.2):

$$\hat{\mathbf{y}} = \frac{\Sigma_i y_i / \epsilon_{si}^2}{\Sigma_i 1/\epsilon_{si}^2} \tag{10}$$

$$\epsilon_{s\hat{y}} = \sqrt{\frac{1}{\Sigma_i 1/\epsilon_{si}^2}}. \tag{11}$$

$\epsilon_{s\hat{y}}$ is the error to the inverse-variance weighted mean, similarly we calculate the combined not scaled SPEXXY errors. The scaling factor and S/N are normal unweighted mean values, while for the quality parameters: distance to the edge, magnitude accuracy, extraction quality flag, and reliability parameter, we keep the minimum value (maximum for the extraction quality flag) included in the combined value. For the log(g) parameter, we give the unweighted mean value, indicating if it was kept fixed or free during the fit. If we used both free/fixed, we give both means.

This leaves us with a combined catalog of 342,797 unique individual stars with physical parameters. We describe recommended quality cuts for using this catalog further in Section 4.7. We match this catalog with the HST catalog by Anderson & van der Marel (2010) but note that 1432 stars in the GTO data, which were extracted using the Anderson et al. (2008) catalog, could not be matched; these stars are included in the catalog without Anderson & van der Marel (2010) magnitudes.

4.4. Membership

To decide which stars likely belong to ω Cen, we assign the stars a membership probability P_M that we can use to exclude foreground or background stars belonging to the Milky Way. We determine this probability using the Python package CLUMPY[16] (Kimmig et al. 2015), which is based on Walker et al. (2009). This code can use either radius and velocity only for the estimate or can include another parameter, like the metallicity, to get the membership probability. As a foreground velocity distribution, we use the Besançon model (Robin et al. 2003)[17] with 1° on each side centered on ω Cen, and the model maximum absolute velocities reach up to 500 km s^{-1}.

The package uses an iterative maximization technique to get the probability and the systemic velocity and dispersion. Three separate memberships are going into the total membership probability, including information about radius, velocity, and the foreground model: (i) the probability of being a member, which assumes that the stars follow a Gaussian velocity distribution centered on the mean velocity of the cluster; (ii) the nonmembership probability including the Besançon model information assuming a velocity dispersion of 20 km s^{-1}; and (iii) the probability depending on the radius assuming a radial decrease in membership. After every iteration, the mean velocity, velocity dispersion, and probability are updated until they converge. We perform 50 iterations, and the initial values

[16] https://github.com/bkimmig/clumpy
[17] https://model.obs-besancon.fr/ws/

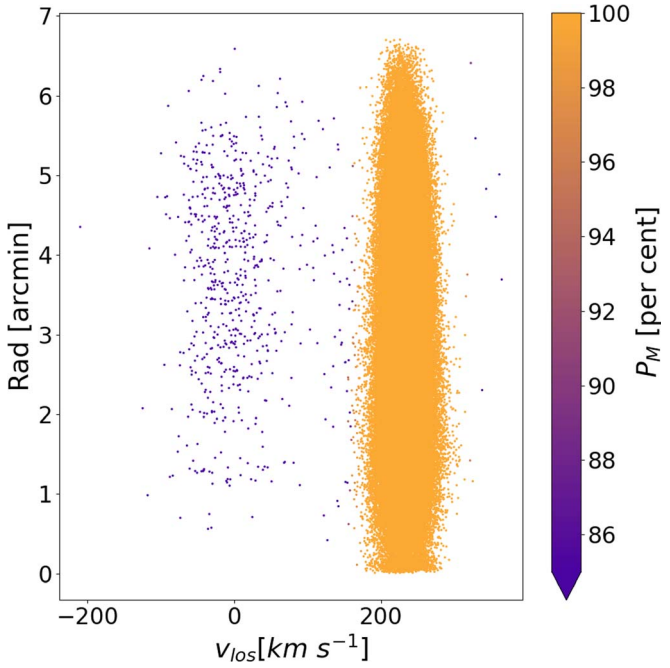

Figure 9. Membership probabilities using radius and velocity for an S/N>10. The stars' radial distances to the cluster center in arcminutes are plotted against their line-of-sight velocities. The points are color coded according to their membership probability, yellow being 1.

are 0.5 for the probabilities and 4 km s^{-1} for the central dispersion of the cluster.

The membership output for S/N > 10 is shown in Figure 9 when using only velocity and radius from the center (R. A.$_c$ = 13:26:47.24 and decl.$_c$ = −47:28:46.45, Anderson & van der Marel 2010) as input. We clearly can see the separation between the foreground stars and the members (over 95% probability) in the velocity radius plane, with 98.8% (338,531 stars) of stars being members and only 1.2% (4266 stars) not. We choose to use the membership that does not include metallicity information for the following analysis since the [M/H] distribution of the cluster is too broad and hence not that easily distinguishable from the foreground. We note that 117 stars have no membership probability since their velocity exceeds the 500 km s^{-1} from the foreground model; however, these stars have low S/N (⩽5).

4.5. Atomic Diffusion Correction

In the left panel of Figure 10 we show the CMD of our full MUSE catalog, with each point colored by its metallicity [M/H]. The stars near the main-sequence turnoff (MSTO) seem to be more metal poor than stars falling directly above and below this region. A similar offset in metallicity was seen by Husser et al. (2016) in NGC 6397, who found a ∼0.3 dex variation in the mean metallicity along the MS, with the lowest metallicity at the turnoff. Other analyses have also found a decrease in the observed metallicity (up to 0.25 dex, King et al. 1998; in M92/NGC 6341) compared to stars of the same population along the MS and subgiant branch (SGB).

This shift can be explained by several internal transport processes including atomic diffusion (gravitational settling of heavier elements), thermal diffusion, radiative acceleration, and turbulent mixing (VandenBerg et al. 2002). For stars evolving through the MSTO, heavier elements begin to sink below the outer layers of the star, causing them to be undetectable via spectroscopy. The consequence is that the observed metallicity of these stars is lower than the abundance they were originally born with. Once a star enters the SGB, convection in the outer layers begins, and heavier elements are then dredged up to the surface where they are once again observable. Therefore, these stars no longer exhibit the offset in metallicity attributed to atomic diffusion. It is also noted in Korn et al. (2007) and Nordlander et al. (2012) that this phenomenon has a larger effect on extremely metal-poor stars, which is where we also see the greatest offset. We note that hereafter we refer to our correction for these effects as an "atomic diffusion correction."

To correct for this effect on our metallicity measurements, we use MIST isochrones (Dotter 2016; Choi et al. 2016), which take into account atomic diffusion. We use the distance modulus for the isochrones and apply extinction and reddening corrections to our photometry. Specifically, we assume A_v = 0.372 mag (Harris 1996; Bellini et al. 2017a) and use the values for A_λ/A_V of 1.34148 and 0.85528 for F435W and F625W respectively,[18] giving us $A_{\lambda,435} = 0.499$ mag and $A_{\lambda,625} = 0.318$ mag. We then subtract A_λ from the relevant magnitudes to obtain our corrected photometry.

We use a series of isochrones with Age = 10 Gyr and $-4.0 < \langle[Fe/H]\rangle < 0.5$. We increase the CMD coverage of the MIST isochrones (which are available in steps of 0.5 to 0.25 dex in metallicity) by interpolating between equivalent evolutionary points to generate isochrones between the given models. We then iterate this process until we obtain good coverage across the CMD and a metallicity precision of 0.03 to 0.06 dex. For each interpolated isochrone, we calculate the difference between its overall metallicity and the surface metallicity at each point along it. We grid these differences in the CMD using color bins of 0.05 mags and F625W bins of 0.12 mags, finding the median correction in each bin. To derive the atomic diffusion (AD) correction for individual stars, we interpolate within this 2D grid of corrections. The bottom panel of Figure 10 shows that these corrections shift the metallicities the most in the MSTO region, while the right panel shows that applying the AD correction narrows the spread in monometallic tracks along the full CMD. We also plot the [M/H] distribution of the RGB stars versus the MSTO (see Figure 11). To aid more direct comparison, we also plot the [M/H] of the RGB with "MSTO-like" errors (meaning for each RGB star, we randomly sample an MSTO star error then resample the given RGB metallicity from a Gaussian with a σ equivalent to the new error. Because RGB metallicities are more well measured, this demonstrates the overall spread in RGB metallicities if they had the same uncertainties as fainter MSTO stars). Before the correction, it is clear that the MSTO stars are shifted to lower metallicities by ∼0.2 dex while after the correction, the distributions are significantly more consistent, as expected.

Using atomic diffusion-corrected metallicities allows us to group stars across the CMD by their birth metallicity, not their observed atmospheric metallicity. This enables us to more accurately group stars with similar abundances and better understand the processes that enrich each population. We include both the raw and atomic diffusion-corrected values for

[18] Obtained from http://stev.oapd.inaf.it/cgi-bin/cmd, see also Girardi et al. (2008).

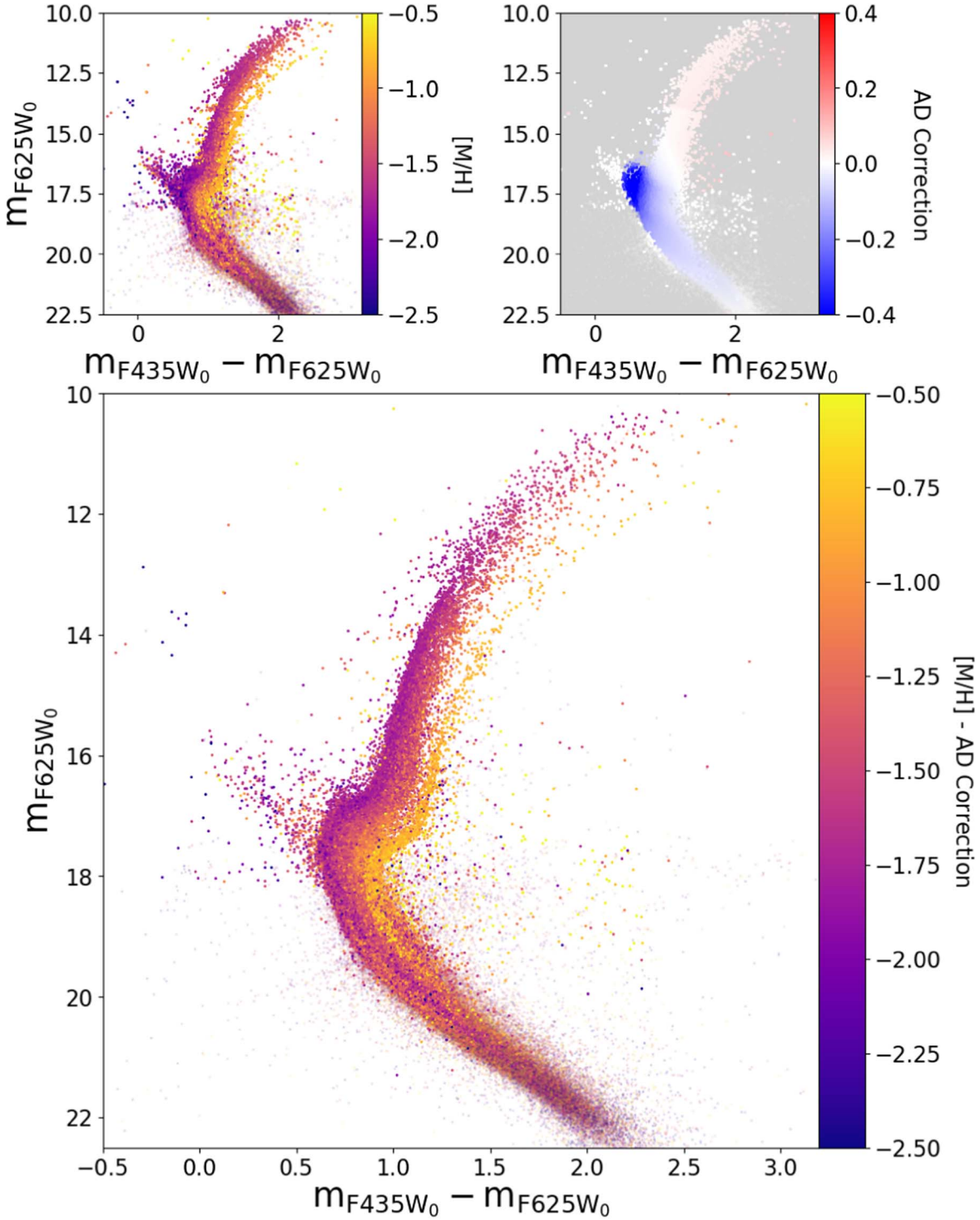

Figure 10. Atomic diffusion correction. Top left: CMD of all stars with HST photometry colored by their metallicity. Top right: a grid of the median metallicity correction when considering isochrones that model atomic diffusion. Bottom: CMD of all stars from the top left panel, now with the relevant atomic diffusion correction applied. Stars with S/N < 10 and less reliable photometry are plotted with transparency in each panel.

the metallicities in our catalog and we use the corrected values in all analyses forthcoming.

4.6. Perspective Rotation

ω Cen takes up a large angle on the plane of the sky. Therefore, there is a non-negligible apparent rotation caused by the different projections of the space motion at different positions on the sky. This is known as perspective rotation (van de Ven et al. 2006). To correct for it we need to subtract from the line-of-sight velocity the perspective rotation term:

$$v_{pr}[\mathrm{km\ s^{-1}}] = 1.3790 \cdot 10^{-3} \cdot D \cdot (-\Delta\mathrm{R.A.} \cdot cos(\mathrm{decl.}) \cdot \mu^{sys}_{\mathrm{R.A.}} + \Delta\mathrm{decl.} \cdot \mu^{sys}_{\mathrm{decl.}}) \quad (12)$$

with the distance to the center ΔR. A. , Δdecl. in units of arcmin, distance to the cluster D=(5.43 $\pm$ 0.05) kpc

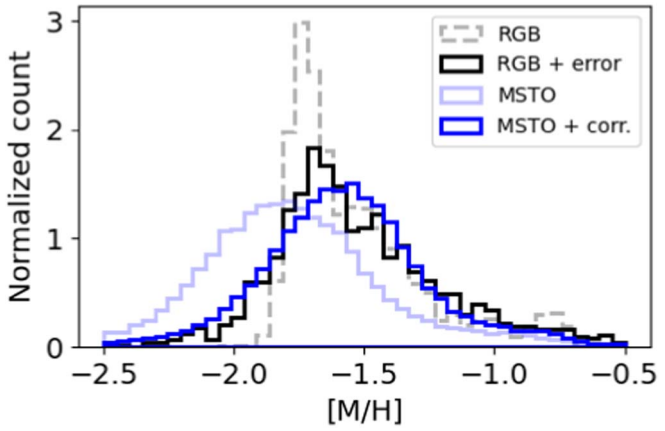

Figure 11. [M/H] of RGB vs. MSTO post AD correction. The figure shows how the atomic diffusion correction causes the [M/H] distribution to be more consistent between the MSTO and the RGB (when considering both to have MSTO-like errors).

(Baumgardt & Vasiliev 2021), proper motion in RA $\mu^{sys}_{\mathrm{R.A.}} = (3.25 \pm 0.022)$ mas yr^{-1} and proper motion in Dec $\mu^{sys}_{\mathrm{decl.}} = (-6.746 \pm 0.022)$ mas yr^{-1} from Vasiliev & Baumgardt (2021).

The resulting velocity calculated with Equation (12) is shown in Figure 12, and the maximum value for the perspective rotation in our data set is 0.35 km s^{-1}.

4.7. Catalog

Having performed all the data reduction, stellar spectra extraction, and analysis steps described in Sections 2, 3 and 4, we have a final spectroscopic catalog with 342,797 stars (GTO: 58,143, GO: 272,633, and combined GO/GTO: 12,021). All the parameters given in this catalog are described in Section E and the S/N of the stars in the CMD is shown in Figure 13. The catalog will be published together with this paper in a machine-readable format.

Since 1,432 GTO stars are not in the Anderson & van der Marel (2010) catalog, they do not have magnitudes in the F625W and F435W filters, and therefore no atomic diffusion correction (ADC) could be performed. We will update the ADC for these stars in a subsequent paper using a new HST catalog (M. Häberle et al. 2023, in preparation) that includes new data acquired under the program GO-16777 (PI: A. Seth).

Our catalog has no quality cuts, as each science case can decide the best cuts for its own purpose. However, the quality cuts we suggest are as follows:

1. Membership probability: $P_M > 95\%$
2. Magnitude accuracy during extraction with PAMPELMUSE $\geqslant 0.6$
3. Reliability: $R \geqslant 0.5$
4. Distance to MUSE IFU edge: $\geqslant 5$ pixel ($1''$)
5. Signal-to-Noise ratio: S/N >10 (see Section B and Section D).

The above cuts yield 156,871 stars, and of these, only 143 GTO stars lack photometry in the Anderson & van der Marel (2010) catalog. These 156,871 stars have a mean metallicity error of 0.15 dex, a median v_{los} error of 6.26 km s^{-1} and a median T_{eff} error of 102 K. In more detail, the mean metallicity error for MS stars (18 mag $<\mathrm{mag}_{F625W} <$ 22 mag) is 0.174 dex, and for RGB stars (16 mag $<\mathrm{mag}_{F625W} <$ 10 mag) is 0.031 dex. We decided on

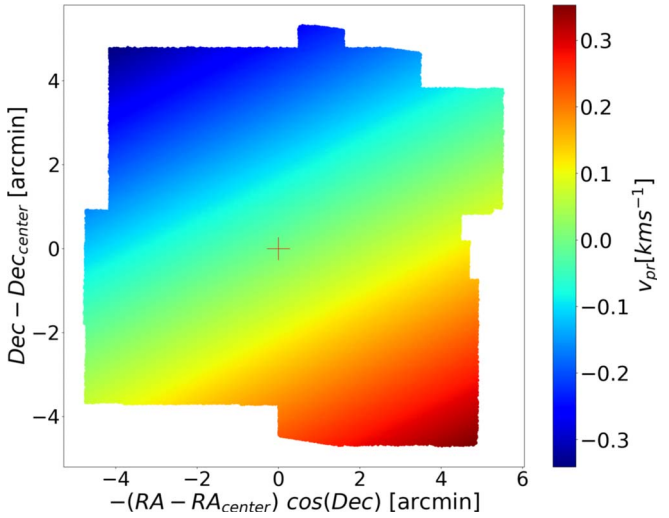

Figure 12. Perspective rotation. The figure shows the position of the data color coded with the perspective rotation value for each star. The red cross indicates the center, and the velocity values increase from the bottom left to the top right corner of the plot.

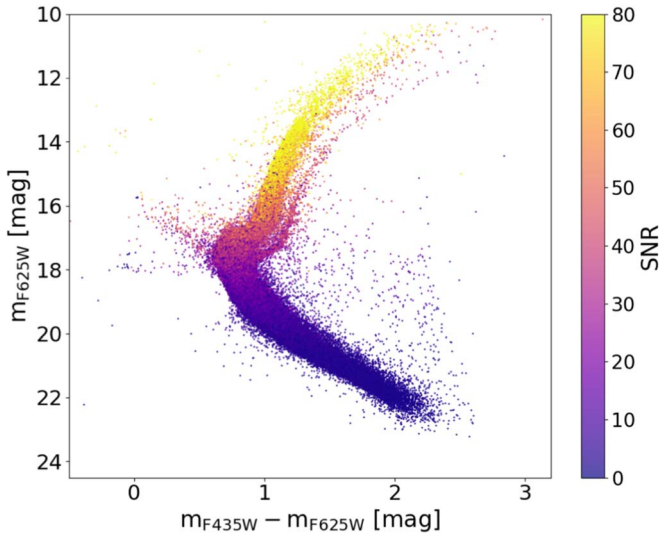

Figure 13. S/N in the catalog. The CMD of the stars in the catalog color coded with their S/N as calculated from SPEXXY.

these cuts in order to have reliable results but still keep as many stars as possible; stricter cuts will give smaller uncertainties. The S/N cut of 10 is consistent with all our tests in Appendices B, C, and D, which show that below that value biases because of different assumptions and setups can play a role. The distance to the edge is chosen to verify that the stars are not outside or exactly at the edge of the IFU, where only part of the starlight can be extracted. The other parameters are reasonable cuts for extraction accuracy, reliability, and membership, but stricter cuts can be applied for higher precision.

Additionally, the median systemic LOS velocity, corrected for the perspective rotation and sign the above quality cuts, is $v_{los} = (232.99 \pm 0.06)$ kms^{-1} with the error found using bootstrapping, and even without the reliability quality cut the result does not change. This value is close to previous values, e.g., (232.7 ± 0.2) kms^{-1} Baumgardt & Hilker (2018) using ESO/VLT, Keck spectra, and literature values, being just slightly out of the 1σ range, while (234.28 ± 0.24) kms^{-1} Baumgardt et al.

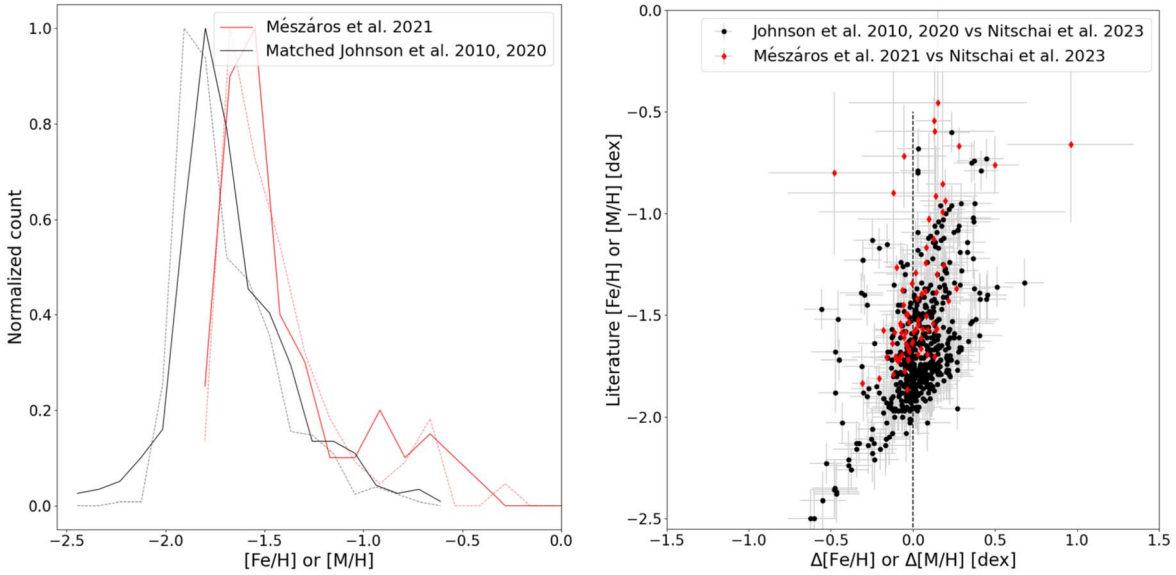

Figure 14. Comparison to literature values. On the left is the [Fe/H] distribution for Johnson & Pilachowski (2010), Johnson et al. (2020), the black solid line, and from the MUSE results, the black dashed line, for all the matched stars in both catalogs. In red is the [M/H] distribution for the matched stars of the Mészáros et al. (2021) data, solid line, and the MUSE data. On the right, we plot the literature values against the difference between the two [Fe/H] or [M/H] values. The black dashed line indicates where both values agree.

(2019) where they used Gaia DR2 data, which due to crowding do not have many stars in the central region where we observe, being outside of the 3σ range due to the small errors.

One should note that these are quality cuts based on our spectroscopic analysis, while the photometry and astrometry are added from the HST catalogs (Sarajedini et al. 2007; Anderson & van der Marel 2010). We are preparing a new astrometric and photometric catalog (M. Häberle et al. 2023, in preparation) that will provide updated values for the magnitudes and positions.

4.8. Literature Comparison

In this subsection, we present a first comparison of our findings with previous works. For the comparison, we use other previous studies that use spectroscopic data and not just photometry.

To compare our [M/H] values from SPEXXY (without AD correction) to literature values for [Fe/H] from RGB stars (e.g., Johnson & Pilachowski 2010; Johnson et al. 2020) we need to transform [M/H] to [Fe/H] values. We use the following formula (Salaris et al. 1993):

$$[\mathrm{Fe/H}] = [\mathrm{M/H}] - \log(0.638 \cdot 10^{[\alpha/\mathrm{Fe}]} + 0.362) \quad (13)$$

with $[\alpha/\mathrm{Fe}]$ set to 0.3 in SPEXXY. This transformation accounts for the contribution of the assumed α enhancement to our assumed [M/H] values, while the literature values derive separate abundances for several α elements (Johnson & Pilachowski 2010).

We match the Johnson & Pilachowski (2010) and Johnson et al. (2020) catalogs to ours using only the brightest stars (F625W $<$ 14 mag) by finding the closest star that is no more than 1″ away, in order to find real matches but not have too strict criteria and eliminate matches due to slight offsets in the coordinates. The [Fe/H] of the 524 matched stars are shown in Figure 14. The measurements are strongly correlated with a mean offset between them of 0.03 dex and a scatter of 0.17 dex, with the literature values being slightly more metal rich but still close to zero showing no strong systematic offset and the scatter representing the statistical discrepancy. We note that our matching criteria and differences in astrometry could result in some mismatched stars. Unfortunately, this cannot easily be improved using photometry, as there are no common filters between the catalogs. In addition, we do not find as low metallicity stars as in Johnson et al. (2020), which seem to have the biggest deviation from our data.

Further, we also match our [M/H] values to the metallicity from Mészáros et al. (2021), where they used APOGEE measurements. Since most of the spectroscopic surveys, like Gaia and APOGEE, have problems with crowding in the central cluster region where we observe, there is almost no overlap. However, we could match 74 stars, and the results are also shown in Figure 14. The measurements have a mean offset between them of 0.06 dex and a scatter of 0.28 dex.

5. Conclusion

In this work, we present an extensive catalog of stars obtained with 87 new MUSE pointings plus the already existing 10 WFM and 6 NFM GTO pointings for ωCen, covering out to the half-light radius.

We describe the data and the analysis steps used to create the final catalog of stars. First, we reduce the data and extract individual spectra of stars using PAMPELMUSE (Kamann et al. 2013). Afterward, we use the spectral fitting routine SPEXXY to measure the LOS velocities, effective temperatures, and metallicities of these stars. We perform multiple tests, including exploiting a large number of repeated measurements to verify our results. We provide several parameters to quantify the reliability of the results and also include several necessary corrections to our measurements. We ended up with 342,797 stars after all of our analysis steps without any quality cuts. However, for most use cases, we suggest several quality cuts: S/N $>$ 10, membership probability $P_M > 0.95\%$, magnitude accuracy $\geqslant 0.6$ mag, distance to the IFU edge $\geqslant 5$, and reliability $R \geqslant 0.5$. Thus, 156,871 stars meet all these criteria.

Finally, we do a first analysis of the metallicity distribution, comparing it to previous works, and find that they are consistent with our findings and calculate the median systematic LOS to be $v_{los} = (\mathbf{2}32.99 \pm 0.06)$ kms^{-1}. A more detailed analysis of the metallicities as well as the LOS velocity information, will be presented in a separate subsequent paper. In addition, a new HST catalog with proper motion photometry for millions of stars covering most of the MUSE data is in preparation (M. Häberle et al. 2023, in preparation). Combining both, the astrometric and spectroscopic catalog for ω Cen, will allow us to measure the ages of the stars and identify the subpopulations of the cluster using photometry and metallicity information (C. Clontz et al. 2023, in preparation). Moreover, using the spectroscopic data we can also measure individual abundances by combining spectra of the same population and directly measuring the absorption lines of different elements (S. Di Stefano et al. 2023, in preparation), which will further constrain the multiple populations and their formation scenario. Combining the information on the stellar populations and kinematics of a large number of stars in ω Cen will provide a clear picture of its formation history.

Acknowledgments

The work is based on observations collected at the European Southern Observatory under ESO program 105.20CG.001. We thank the ESO staff for their excellent support. Also based on observations made with the NASA/ESA Hubble Space Telescope, obtained from the data archive at the Space Telescope Science Institute. STScI is operated by the Association of Universities for Research in Astronomy, Inc. under NASA contract NAS 5-26555. This research made use of NASA's Astrophysics Data System. A.S., C.C. and M.A.C. acknowledge support from HST grant GO-16777. We acknowledge funding from the Deutsche Forschungsgemeinschaft (grant LA 4383/4-1 and DR 281/35-1) and from the German Ministry for Education and Science (BMBF Verbundforschung) through grants 05A14MGA, 05A17MGA, and 05A20MGA. S.K. acknowledges funding from UKRI in the form of a Future Leaders Fellowship (grant No. MR/T022868/1). We thank the anonymous referee for the helpful and constructive comments.

Facilities: VLT Yepun (MUSE), HST (ACS).

Software: PAMPELMUSE (Kamann et al. 2013), SPEXXY v5.2.21 (https://github.com/thusser/spexxy), ASTROPY v5.2.1 (Astropy Collaboration et al. 2013, 2018, 2022), CLUMPY (Kimmig et al. 2015), MATPLOTLIB v3.7.1 (Hunter 2007; Caswell et al. 2023), PANDAS v1.5.3 (McKinney 2010; The Pandas Development Team 2023), NUMPY v1.20.3 (Harris et al. 2020), SCIPY v.1.10.1 (Virtanen et al. 2020), MUSE pipeline v2.8.3 (Weilbacher et al. 2016, 2020). In the Appendix, we include further information and elaborate on checks we performed on our data.

Appendix A
Data Conditions

Since our data were taken over an extended period of longer than a year, the atmospheric conditions were also varying. In Table 2 we summarize the conditions and observing date of the individual GO pointings used in this analysis. We requested an airmass of less than 1.4 and seeing below 0.″8, which were almost always fulfilled.

Table 2
Observing Conditions

OB	Date	Average Airmass	Average Seeing
1.1	2021 Feb 17	1.263	0.897
1.2	2021 Feb 17	1.246	0.777
1.3	2021 Feb 17	1.204	0.733
1.3[a]	2022 Sep 2	2.144	0.577
2.1	2021 Mar 16	1.102	1.203
2.2	2021 Mar 16	1.092	1.133
2.3	2021 Mar 16	1.087	1.357
3.1	2021 Mar 16	1.088	1.097
3.2	2021 Mar 16	1.093	1.127
3.3	2021 Mar 16	1.103	1.360
4.1	2021 Apr 8	1.096	0.433
4.2	2021 Apr 8	1.089	0.500
4.3	2021 Apr 8	1.086	0.470
5.1	2021 Mar 14	1.088	1.140
5.2	2021 Mar 14	1.094	1.110
5.3	2021 Mar 14	1.103	1.133
5.4	2021 Mar 14	1.116	1.273
6.1	2021 Apr 8	1.088	0.503
6.2	2021 Apr 8	1.093	0.527
6.3	2021 Apr 8	1.101	0.497
6.4	2021 Apr 8	1.113	0.547
7.1	2021 May 18	1.209	0.567
7.2	2021 May 18	1.180	0.547
7.3	2021 May 18	1.155	0.553
7.4	2021 May 18	1.135	0.450
8.1	2021 May 18	1.089	0.59
8.2	2021 May 18	1.086	0.573
8.3	2021 May 18	1.087	0.687
9.1	2021 Jun 30	1.088	0.883
9.2	2021 Jun 30–Jul 1	1.093	0.907
9.3	2021 Jul 1	1.101	1.147
9.4	2021 Jul 1	1.113	1.163
10.1	2021 Jul 4	1.106	0.937
10.2	2021 Jul 4	1.119	0.877
10.3	2021 Jul 4	1.119	0.843
10.4	2021 Jul 4	1.157	0.840
11.1	2022 Mar 31	1.295	0.62
11.2	2022 Mar 31	1.253	0.540
11.3	2022 Mar 31	1.217	0.50
11.4	2022 Mar 31	1.186	0.4340
12.1	2022 Feb 9	1.325	0.557
12.2	2022 Feb 9	1.279	0.677
12.3	2022 Feb 9	1.239	0.637
12.4	2022 Feb 9	1.206	0.700
13.1	2022 Feb 9	1.171	0.507
13.2	2022 Feb 9	1.148	0.703
13.3	2022 Feb 9	1.128	0.563
13.4	2022 Feb 9	1.113	0.693
14.1	2022 Feb 9	1.099	0.723
14.2	2022 Feb 9	1.091	1.020
14.3	2022 Feb 9	1.087	0.650
14.4	2022 Feb 9	1.085	0.780
15.1	2022 Feb 10	1.250	0.653
15.2	2022 Feb 10	1.215	0.727
15.3	2022 Feb 10	1.184	0.823
15.4	2022 Feb 10	1.159	0.597
16.1	2022 Feb 10	1.133	0.740
16.2	2022 Feb 10	1.117	0.600
16.3	2022 Feb 10	1.103	0.433
16.4	2022 Feb 10	1.094	0.897
17.1	2022 Feb 27	1.358	0.350
17.2	2022 Feb 27	1.308	0.307
17.3	2022 Feb 27	1.265	0.293
17.4	2022 Feb 27	1.228	0.250

Table 2
(Continued)

OB	Date	Average Airmass	Average Seeing
18.1	2022 Feb 27	1.090	0.387
18.2	2022 Feb 27	1.086	0.413
18.3	2022 Feb 27	1.086	0.357
18.4	2022 Feb 27	1.089	0.520
19.1	2022 Feb 27	1.100	0.437
19.2	2022 Feb 27–28	1.147	0.463
19.3	2022 Feb 28	1.201	0.500
19.4	2022 Feb 28	1.173	0.627
20.1	2022 Feb 28	1.143	0.493
20.2	2022 Feb 28	1.125	0.397
20.3	2022 Feb 28	1.110	0.380
20.4	2022 Feb 28	1.100	0.380
21.1	2022 Feb 28	1.360	0.413
21.2	2022 Feb 28	1.087	0.453
21.3	2022 Feb 28	1.087	0.373
21.4	2022 Feb 28	1.091	0.307
22.1	2022 Mar 2	1.379	0.640
22.2	2022 Mar 2	1.326	0.517
22.3	2022 Mar 2	1.280	0.567
22.4	2022 Mar 2	1.241	0.877
23.1	2022 Mar 2	1.114	0.487
23.2	2022 Mar 2	1.102	0.493
23.3	2022 Mar 2	1.094	0.437
23.4	2022 Mar 2	1.089	0.463

Notes. The observing conditions for all GO observations used in our work. OB: the name/numbering of the individual pointings. Date: the date of observation. Average airmass: the mean airmass at the start of each of the three rotated exposures. Average seeing: the mean seeing at the start of the three rotated exposures for one OB. OB 1.3 was observed twice since the offset of the pointing was not correct and created a gap in our continuous coverage.
[a] OB 1.3 was observed twice since it had a wrong offset causing a gap in our data set.

Appendix B
PAMPELMUSE Tests

We verify that slightly changing the PAMPELMUSE setup does not influence our results for stars with $S/N > 10$. For these tests, we use two example pointings where a different setting might have been more appropriate. First, we use a round PSF, fixing the ellipticity to 0, for OB 15.3, since the free Moffat PSF we generally use seems unnecessarily complex as it is round anyway. For the second example, we used OB 21.2 and masked certain layers in the wavelength range that appear to have something wrong with them, bad pixels from the data reduction, since their values drop significantly compared to the rest of the spectrum. The results show no significant difference in the SPEXXY output for an $S/N > 10$, even though the new setup should be better for these two cases. Therefore, we keep the setup consistent for all OBs as described in Section 3.1.

Appendix C
Surface Gravity log(g)

In this section of the Appendix, we investigate the bias we have due to the fixed log(g) parameter from one single isochrone for most stars (see Section 3.3).

C.1. Free log(g)

First, we investigate how allowing log(g) to vary freely for all stars during the fit with SPEXXY, would change our results. For that, we look at a subset of our data, including RGB and MS stars, which gives us a complete representation of the magnitude and S/N range.

The deviations between the free and fixed log(g) fit are shown in Figure 15. Most of the results are within the 3σ range for an $S/N > 10$. The deviations at high S/N are because of the smaller errors at that level. We can see that all parameters tend to get lower when the log(g) values are left free, but not as significant for [M/H] and v_{los} where they almost all stay within the 3σ range. This also proves that the log(g) parameter does not affect the metallicity calculation strongly.

C.2. Metal-rich Stars

Since the cluster is known to have multiple populations, we know that one isochrone for finding the log(g) is not ideal. To investigate the bias we have because of that, we test one extreme population, the metal-rich stars with $[M/H] > -1$ dex, and use a different isochrone, more representative for them, and assign them new log(g) values.

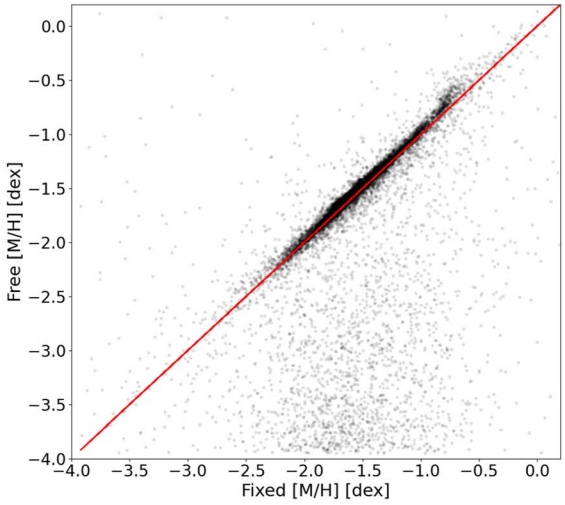

(a) [M/H] comparison

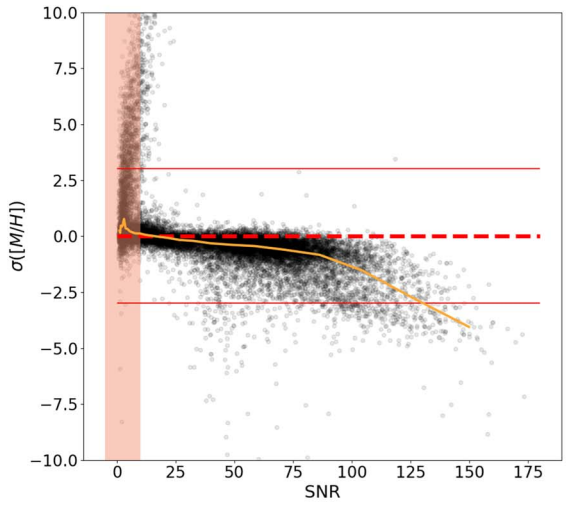

(b) [M/H] sigma discrepancy

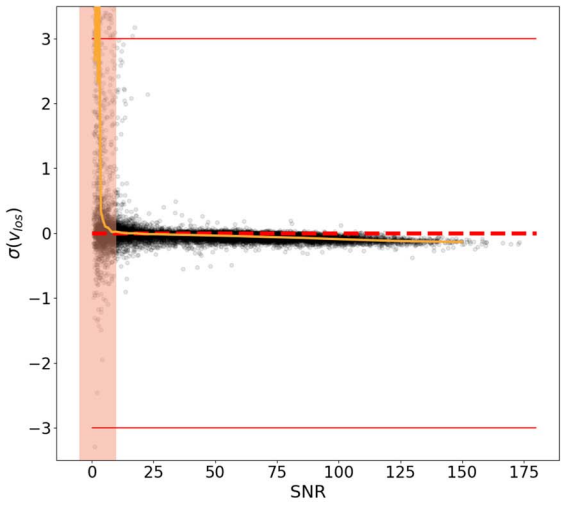

(c) v_{los} sigma discrepancy

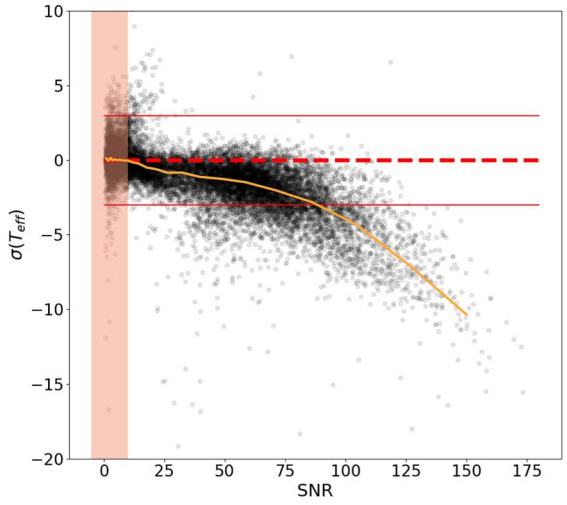

(d) T_{eff} sigma discrepancy

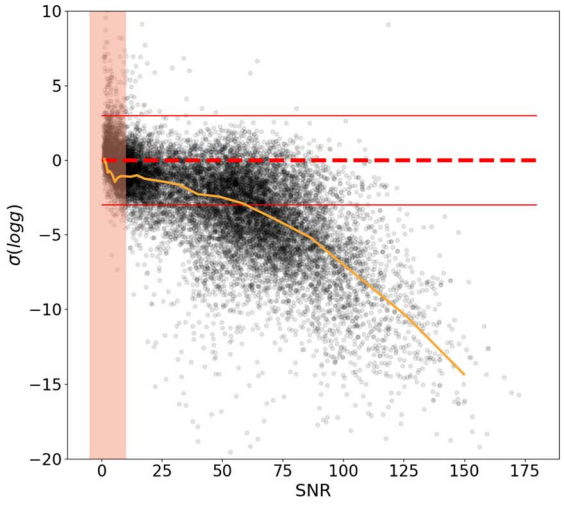

(e) log(g) sigma discrepancy

Figure 15. The discrepancy between spectral parameters with free and fixed log(g). (a) The one-to-one comparison between the [M/H] values, the red line as the 1 to 1 ratio. (b)–(e) The σ deviations for [M/H], v_{los}, T_{eff}, and log(g). We divide the difference between the two results with the scale error in our catalog, except for the log (g), where we take the SPEXXY error for the free log(g) run. The dashed red line is at 0, the solid red lines are at the 3σ limits, and the orange solid line is the median of all stars, while the red shaded area is the S/N limit of 10.

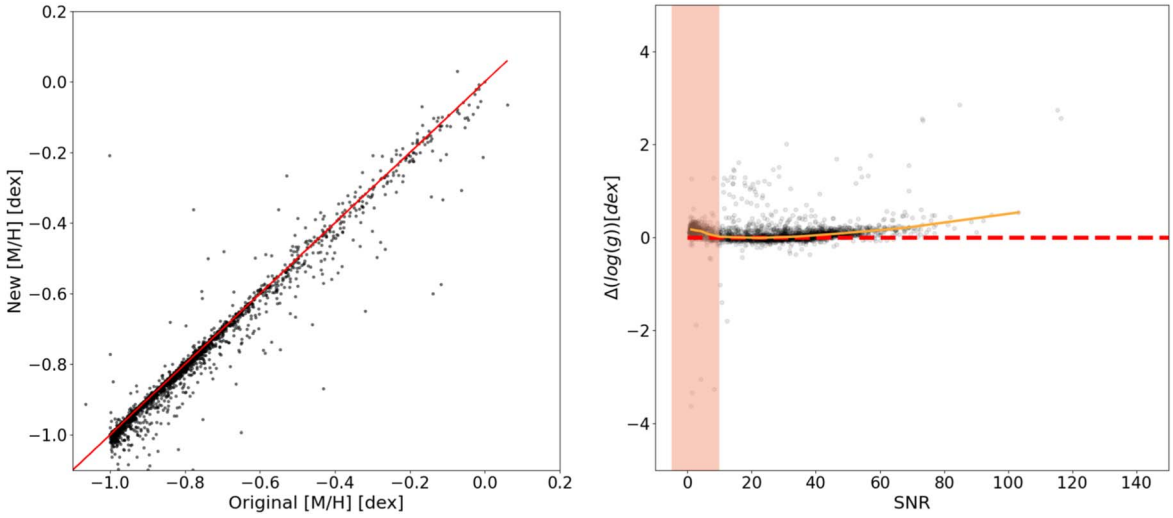

Figure 16. Metal rich. On the left plot, the one-to-one comparison of the [M/H] is shown, with the red solid line being the 1 to 1 ratio. On the right is the difference in log(g) between the two isochrones, with the dashed line indicating no difference at all, the orange line the median difference of our data, and the red shaded area the S/N limit of 10.

In Figure 16 the [M/H] results are shown, and the difference between the log(g). In general, there seems to be just a small difference in log(g) even with a different isochrone and a tight one-to-one correlation between the [M/H], reassuring us that the exact isochrone used for the initial guesses and log(g) values is not that significant.

C.3. Literature log(g)

Using the matching between Johnson & Pilachowski (2010), Johnson et al. (2020), Mészáros et al. (2021), and our catalog, described in Section 4.8, we also compare our surface gravity values with the literature. Almost all values are for a fixed log (g) from the isochrone described in Section 3.3.

The log(g) of the matched stars is shown in Figure 17. The measurements have a mean offset between that of Johnson & Pilachowski (2010) and Johnson et al. (2020) of 0.18 dex and a scatter of 0.26 dex, with the literature values having slightly lower log(g) values. With the Mészáros et al. (2021) values, the mean offset is 0.04 dex and a scatter of 0.46 dex. This shows that even though our initial isochrone is not a perfect match for all stars, because of multiple populations and binaries, it still gives reasonable log(g) values since they are comparable to previous studies. In addition, the metallicity values also are within the expected literature range (see Section 4.8) even though log(g) is fixed, hence this is another indication that there is no strong effect, as already suggested in Husser et al. (2016), Kamann et al. (2016) and in Section C.1, Section C.2.

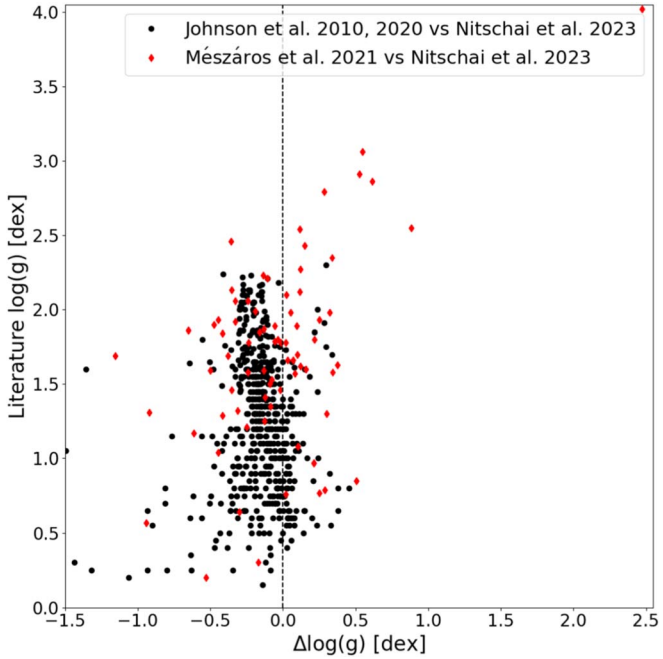

Figure 17. Literature comparison log(g). We plot the literature values against the difference between the literature and our log(g) values.

Appendix D
S/N Test

To make sure that we have no bias in our metallicity and velocity measurements for stars with different S/N, we performed another test, adding different noise values to the spectra and redoing the SPEXXY fit.

We selected randomly 147 spectra with S/N above 28 (being not on the HB) and added Gaussian noise, creating 3999 spectra with S/N between 1 and the original S/N. The difference between the original SPEXXY results and the new ones with more noise increases as expected for lower S/N, and the output errors also increase. The σ difference as a function of the new S/N is shown in Figure 18. Almost all results are within the 3σ range for S/N > 10, and we do not see any bias toward higher or lower values for lower S/N.

The σ difference is calculated using the error directly from SPEXXY. If we also apply the error correction as described in Section 4.2, the difference even decreases.

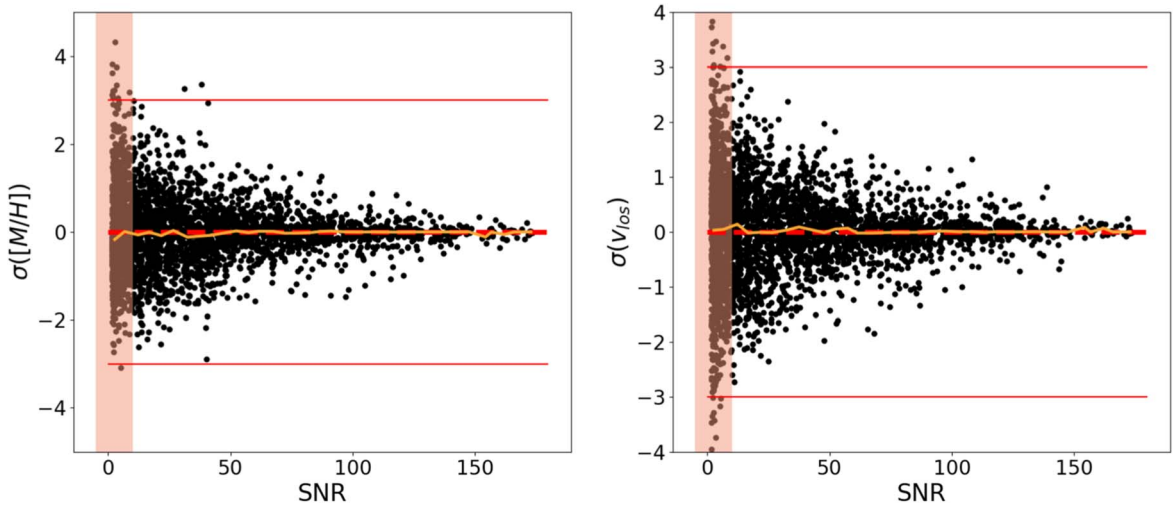

Figure 18. S/N test. The left plot shows on the y-axis the σ difference between the original result and the different [M/H] results after adding noise to the spectra, and the x-axis is the new S/N with the added noise. Similar for the right plot but for the v_{los} values. The light red shaded areas indicate S/N below 10, the red solid horizontal lines are the 3σ difference, the red dashed horizontal lines are at 0, and the orange solid lines are the median values for our measurements as a function of S/N.

Appendix E
Catalog Columns

Table 3 lists all parameters given in the spectroscopic catalog described in this paper. The entries in the catalog are sorted by increasing radius from the center.

Table 3
Catalog

Column Name	Description	More Details	Units
MUSE	Identifier of stars in spectroscopic catalog		
RVel	Line-of-sight velocity (v_{los})	SPEXXY output	km s^{-1}
errRVel	SPEXXY line-of-sight velocity uncertainty ($\epsilon_{v_{los}}$)	SPEXXY output	km s^{-1}
sRVel	Scaling factor for $\epsilon_{v_{los}}$	Section 4.2	
e_RVel	Scaled error v_{los}	Section 4.2	km s^{-1}
prv	Perspective rotation	see Section 4.6 and van de Ven et al. (2006)	km s^{-1}
prvRVel	v_{los} corrected for perspective rotation	see Section 4.6 and van de Ven et al. (2006)	km s^{-1}
Teff	Effective Temperature (T_{eff})	SPEXXY output	K
errTeff	SPEXXY effective Temperature uncertainty ($\epsilon_{T_{eff}}$)	SPEXXY output	K
sTeff	Scaling factor for $\epsilon_{T_{eff}}$	Section 4.2	
e_Teff	Scaled error T_{eff}	Section 4.2	K
loggfix	Fixed surface gravity (log(g))	Isochrone output (Section 3.3)	[cm/s^2]
loggfree	Fitted surface gravity (log(g))	SPEXXY output	[cm/s^2]
MH	Metallicity ([M/H])	SPEXXY output	[Sun]
MHadc	Metallicity corrected for AD	see Section 4.5	[Sun]
errMH	SPEXXY metallicity uncertainty ($\epsilon_{[M/H]}$)	SPEXXY output	[Sun]
sMH	Scaling factor for $\epsilon_{[M/H]}$	Section 4.2	
e_MH	Scaled error [M/H]	Section 4.2	[Sun]
SNR	Signal-to-noise ratio (S/N)	SPEXXY output	
ffit	Fixed or free log(g) in SPEXXY	0 free and 1 fixed	
edge	Distance of star to OB edge	PAMPELMUSE output	pixel
Magacc	Relative accuracy of recovered magnitude from spectrum extraction	PAMPELMUSE output	
SpecFlag	Spectrum extraction quality flag	PAMPELMUSE output	
Rel	Reliability Parameter R	Section 4.1	
Num	Number of times the star was observed	Section 4.3	
Data	Observing program (GO/GTO) the star belongs to	GTO, GO, or both (GO_GTO)	
Rad	Radius from cluster center	$\sqrt{((\text{R.A.}-\text{R.A.}_c)cos(\text{decl.}))^2 + (\text{decl.}-\text{decl.}_c)^2}$	deg
RAdeg	Right ascension	Sarajedini et al. (2007); Anderson et al. (2008), Anderson & van der Marel (2010)	deg
DEdeg	decl.	Sarajedini et al. (2007); Anderson et al. (2008), Anderson & van der Marel (2010)	deg
435mag	Magnitude in the F435W filter (Vega)	Anderson & van der Marel (2010)	mag
625mag	Magnitude in the F625W filter (Vega)	Anderson & van der Marel (2010)	mag
435magC	F435W-band photometry (Vega)	A_V and R_V Correction Applied	mag
625magC	F625W-band photometry (Vega)	A_V and R_V Correction Applied	mag
e_435mag	RMS scatter of single-exposure F435W observation	Anderson & van der Marel (2010)	mag
e_625mag	RMS scatter of single-exposure F625W observation	Anderson & van der Marel (2010)	mag
NBf	Number of F435W images where star was found	Anderson & van der Marel (2010)	
NRf	Number of F625W images where star was found	Anderson & van der Marel (2010)	
probRV	Membership probability	radius and velocity (Section 4.4)	
probRVM	Membership probability	radius, velocity, and [M/H]	
Flag	Quality Flag	1 = True, 0 = False, see Section 4.7	
HST10Flag	HST quality flag for Anderson & van der Marel (2010)	1 = reliable, 0 = unreliable photometry/astrometry	

Notes. R.A.$_c$ = 13:26:47.24 and decl.$_c$ = −47:28:46.45 (Anderson & van der Marel 2010). For the parameter's edge, Magacc, SpecFlag, and Rel, we provide the minimum (maximum for SpecFlag) value when combining multiple measures; see Section 4.3.

(This table is available in its entirety in machine-readable form.)

ORCID iDs

M. S. Nitschai https://orcid.org/0000-0002-2941-4480
N. Neumayer https://orcid.org/0000-0002-6922-2598
C. Clontz https://orcid.org/0009-0005-8057-0031
M. Häberle https://orcid.org/0000-0002-5844-4443
A. C. Seth https://orcid.org/0000-0003-0248-5470
T.-O. Husser https://orcid.org/0000-0003-2466-5077
S. Kamann https://orcid.org/0000-0001-6604-0505
M. Alfaro-Cuello https://orcid.org/0000-0002-1212-2844
A. Bellini https://orcid.org/0000-0003-3858-637X

S. Dreizler https://orcid.org/0000-0001-6187-5941
A. Feldmeier-Krause https://orcid.org/0000-0002-0160-7221
M. Latour https://orcid.org/0000-0002-7547-6180
M. Libralato https://orcid.org/0000-0001-9673-7397
A. P. Milone https://orcid.org/0000-0001-7506-930X
R. Pechetti https://orcid.org/0000-0002-1670-0808
G. van de Ven https://orcid.org/0000-0003-4546-7731
K. Voggel https://orcid.org/0000-0001-6215-0950
Daniel R. Weisz https://orcid.org/0000-0002-6442-6030

References

Alfaro-Cuello, M., Kacharov, N., Neumayer, N., et al. 2019, ApJ, 886, 57
Alfaro-Cuello, M., Kacharov, N., Neumayer, N., et al. 2020, ApJ, 892, 20
Allende Prieto, C., Majewski, S. R., Schiavon, R., et al. 2008, AN, 329, 1018
Anderson, A. J. 1997, PhD thesis, Univ. California
Anderson, J., Sarajedini, A., Bedin, L. R., et al. 2008, AJ, 135, 2055
Anderson, J., & van der Marel, R. P. 2010, ApJ, 710, 1032
Arsenault, R., Madec, P. Y., Hubin, N., et al. 2010, Proc. SPIE, 7736, 77360L
Astropy Collaboration, Robitaille, T. P., Tollerud, E. J., et al. 2013, A&A, 558, A33
Astropy Collaboration, Price-Whelan, A. M., Sipőcz, B. M., et al. 2018, AJ, 156, 123
Astropy Collaboration, Price-Whelan, A. M., Lim, P. L., et al. 2022, ApJ, 935, 167
Bacon, R., Accardo, M., Adjali, L., et al. 2010, Proc. SPIE, 7735, 773508
Bacon, R., Vernet, J., Borisova, E., et al. 2014, Msngr, 157, 13
Baumgardt, H., & Hilker, M. 2018, MNRAS, 478, 1520
Baumgardt, H., Hilker, M., Sollima, A., & Bellini, A. 2019, MNRAS, 482, 5138
Baumgardt, H., & Vasiliev, E. 2021, MNRAS, 505, 5957
Bedin, L. R., Piotto, G., Anderson, J., et al. 2004, ApJL, 605, L125
Bekki, K., & Freeman, K. C. 2003, MNRAS, 346, L11
Bellini, A., Anderson, J., van der Marel, R. P., et al. 2017a, ApJ, 842, 7
Bellini, A., Bedin, L. R., Piotto, G., et al. 2010, AJ, 140, 631
Bellini, A., Milone, A. P., Anderson, J., et al. 2017b, ApJ, 844, 164
Buder, S., Sharma, S., Kos, J., et al. 2021, MNRAS, 506, 150
Caswell, T. A., Lee, A., Sales De Andrade, E., et al., 2023 matplotlib/matplotlib: REL: v3.7.1, v v3.7.1, Zenodo, doi:10.5281/zenodo.7697899
Choi, J., Dotter, A., Conroy, C., et al. 2016, ApJ, 823, 102
De Silva, G. M., Freeman, K. C., Bland-Hawthorn, J., et al. 2015, MNRAS, 449, 2604
Deng, L.-C., Newberg, H. J., Liu, C., et al. 2012, RAA, 12, 735
Dotter, A. 2016, ApJS, 222, 8
Elson, R. A. W., Gilmore, G. F., Santiago, B. X., & Casertano, S. 1995, AJ, 110, 682
ESO CPL Development Team, 2015 EsoRex: ESO Recipe Execution Tool, Astrophysics Source Code Library, ascl:1504.003
Fahrion, K., Lyubenova, M., van de Ven, G., et al. 2021, A&A, 650, A137
Freeman, K. C., & Rodgers, A. W. 1975, ApJL, 201, L71
Gaia Collaboration, Prusti, T., de Bruijne, J. H. J., et al. 2016, A&A, 595, A1
Georgiev, I. Y., & Böker, T. 2014, MNRAS, 441, 3570
Giesers, B., Kamann, S., Dreizler, S., et al. 2019, A&A, 632, A3
Girardi, L., Dalcanton, J., Williams, B., et al. 2008, PASP, 120, 583
Harris, C. R., Millman, K. J., van der Walt, S. J., et al. 2020, Natur, 585, 357
Harris, W. E. 1996, AJ, 112, 1487
Haywood, M., Di Matteo, P., Lehnert, M. D., et al. 2018, ApJ, 863, 113
Helmi, A., Babusiaux, C., Koppelman, H. H., et al. 2018, Natur, 563, 85
Helmi, A., & White, S. D. M. 2001, MNRAS, 323, 529
Hilker, M., Kayser, A., Richtler, T., & Willemsen, P. 2004, A&A, 422, L9
Hunter, J. D. 2007, CSE, 9, 90
Husser, T.-O., Kamann, S., Dreizler, S., et al. 2016, A&A, 588, A148
Husser, T.-O., Latour, M., Brinchmann, J., et al. 2020, A&A, 635, A114
Husser, T.-O., Wende-von Berg, S., Dreizler, S., et al. 2013, A&A, 553, A6
Ibata, R. A., Bellazzini, M., Malhan, K., Martin, N., & Bianchini, P. 2019, NatAs, 3, 667
Ibata, R. A., Wyse, R. F. G., Gilmore, G., Irwin, M. J., & Suntzeff, N. B. 1997, AJ, 113, 634
Johnson, C. I., Dupree, A. K., Mateo, M., et al. 2020, AJ, 159, 254
Johnson, C. I., & Pilachowski, C. A. 2010, ApJ, 722, 1373
Joo, S.-J., & Lee, Y.-W. 2013, ApJ, 762, 36
Kacharov, N., Alfaro-Cuello, M., Neumayer, N., et al. 2022, ApJ, 939, 118
Kacharov, N., Neumayer, N., Seth, A. C., et al. 2018, MNRAS, 480, 1973
Kamann, S., Husser, T. O., Brinchmann, J., et al. 2016, A&A, 588, A149
Kamann, S., Husser, T. O., Dreizler, S., et al. 2018, MNRAS, 473, 5591
Kamann, S., Wisotzki, L., & Roth, M. M. 2013, A&A, 549, A71
Kimmig, B., Seth, A., Ivans, I. I., et al. 2015, AJ, 149, 53
King, J. R., Stephens, A., Boesgaard, A. M., & Deliyannis, C. 1998, AJ, 115, 666
Korn, A. J., Grundahl, F., Richard, O., et al. 2007, ApJ, 671, 402
Kruijssen, J. M. D., Pfeffer, J. L., Reina-Campos, M., Crain, R. A., & Bastian, N. 2019, MNRAS, 486, 3180
Laporte, C. F. P., Johnston, K. V., Gómez, F. A., Garavito-Camargo, N., & Besla, G. 2018, MNRAS, 481, 286
Latour, M., Calamida, A., Husser, T. O., et al. 2021, A&A, 653, L8
Latour, M., Hämmerich, S., Dorsch, M., et al. 2023, A&A, 677, A86
Limberg, G., Souza, S. O., Pérez-Villegas, A., et al. 2022, ApJ, 935, 109
Majewski, S. R., Nidever, D. L., Smith, V. V., et al. 2012, ApJL, 747, L37
Majewski, S. R., Schiavon, R. P., Frinchaboy, P. M., et al. 2017, AJ, 154, 94
Marigo, P., Girardi, L., Bressan, A., et al. 2017, ApJ, 835, 77
Mayer, L., Moore, B., Quinn, T., Governato, F., & Stadel, J. 2002, MNRAS, 336, 119
Mayor, M., Duquennoy, A., Udry, S., Andersen, J., & Nordstrom, B. 1996, in ASP Conf. Ser. 90, The Origins, Evolution, and Destinies of Binary Stars in Clusters, ed. E. F. Milone & J. C. Mermilliod (San Francisco, CA: ASP), 190
McKinney, W. 2010, in Proc. of the 9th Python in Science Conf. (SciPy 2010), ed. S. van der Walt & J. Millman (Austin, TX: SciPy), 56
Mészáros, S., Masseron, T., Fernández-Trincado, J. G., et al. 2021, MNRAS, 505, 1645
Milone, A. P., Marino, A. F., Bedin, L. R., et al. 2017, MNRAS, 469, 800
Moffat, A. F. J. 1969, A&A, 3, 455
Neumayer, N., Seth, A., & Böker, T. 2020, A&ARv, 28, 4
Nordlander, T., Korn, A. J., Richard, O., & Lind, K. 2012, ApJ, 753, 48
The Pandas Development Team, 2023 pandas-dev/pandas: Pandas, v1.5.3, Zenodo, doi:10.5281/zenodo.7549438
Pechetti, R., Kammann, S., Krajnović, D., et al. 2023, MNRAS, submitted
Pfeffer, J., & Baumgardt, H. 2013, MNRAS, 433, 1997
Pfeffer, J., Griffen, B. F., Baumgardt, H., & Hilker, M. 2014, MNRAS, 444, 3670
Robin, A. C., Reylé, C., Derrière, S., & Picaud, S. 2003, A&A, 409, 523
Salaris, M., Chieffi, A., & Straniero, O. 1993, ApJ, 414, 580
Sánchez-Janssen, R., Côté, P., Ferrarese, L., et al. 2019, ApJ, 878, 18
Sarajedini, A., Bedin, L. R., Chaboyer, B., et al. 2007, AJ, 133, 1658
Siegel, M. H., Dotter, A., Majewski, S. R., et al. 2007, ApJL, 667, L57
Stewart, K. R., Bullock, J. S., Wechsler, R. H., Maller, A. H., & Zentner, A. R. 2008, ApJ, 683, 597
Streicher, O., 2016 Python-CPL: Python interface for the ESO Common Pipeline Library, Astrophysics Source Code Library, ascl:1612.001
Ströbele, S., La Penna, P., Arsenault, R., et al. 2012, Proc. SPIE, 8447, 844737
Tonry, J., & Davis, M. 1979, AJ, 84, 1511
VandenBerg, D. A., Richard, O., Michaud, G., & Richer, J. 2002, ApJ, 571, 487
van de Ven, G., van den Bosch, R. C. E., Verolme, E. K., & de Zeeuw, P. T. 2006, A&A, 445, 513
Vasiliev, E., & Baumgardt, H. 2021, MNRAS, 505, 5978
Villanova, S., Geisler, D., Gratton, R. G., & Cassisi, S. 2014, ApJ, 791, 107
Villanova, S., Piotto, G., King, I. R., et al. 2007, ApJ, 663, 296
Virtanen, P., Gommers, R., Oliphant, T. E., et al. 2020, NatMe, 17, 261
Walker, M. G., Mateo, M., Olszewski, E. W., Sen, B., & Woodroofe, M. 2009, AJ, 137, 3109
Weilbacher, P. M., Streicher, O., & Palsa, R., 2016 MUSE-DRP: MUSE Data Reduction Pipeline, Astrophysics Source Code Library, ascl:1610.004
Weilbacher, P. M., Palsa, R., Streicher, O., et al. 2020, A&A, 641, A28